In situ stress profiling along Bedretto boreholes via integrated geomechanical approaches

Master Thesis

Author(s):
Stadler, Deborah

Publication date:
2022

Permanent link:
https://doi.org/10.3929/ethz-b-000592213

ETH
Eidgenössische Technische Hochschule Zürich
Swiss Federal Institute of Technology Zurich

DERDW
EARTH SCIENCES

Deborah Stadler

In situ stress profiling along Bedretto boreholes via integrated geomechanical approaches

Master Thesis

Chair of Engineering Geology
Geological Institute
Swiss Federal Institute of Technology (ETH) Zurich

Supervision

First Supervisor
Dr. Xiaodong Ma

Co-Supervisors
Dr. Marian Hertrich
Dr. Shihuai Zhang
Kai Bröker

November 30, 2022

Abstract

With the Bedretto Underground Laboratory for Geoscience, ETH Zurich has an excellent opportunity to gain a deeper insight into underground processes relevant for hydro-seismo-mechanical fractured granitic rock mass behaviour and subsequent applications. Improvement of state-of-the-art equipment and research progress in geothermal energy, earthquake physics and rock stability can be achieved by conducting essential experiments directly into the fractured crystalline underground. In an unique research infrastructure, it is possible to overcome the challenging transfer from small laboratory experiments to large-scale reservoir projects.

Within this work, the in-situ stress was mapped and characterised along three inclined boreholes of varying lengths (2 x 40 m and 216.5 m) in the Bedretto tunnel using two different methods: Mini-frac tests and Ellipticity analysis. The two methods focus on the local in-situ stress estimation and complement each other to improve understanding of the in-situ stress state.

The Mini-frac experiments were conducted to infer the minimum principal stress magnitude from fracture closure, shut-in and jacking pressure. In summary, the minimum principal stress has been most accurately estimated from the shut-in pressure. Based on the pressure decay analysis after the shut-in, a minimum principal stress of 15.6 $\pm$ 2.8 MPa was measured using the inflection point method inside the short boreholes. An increase of the pore pressure with the depth from 2.5 to 3.7 MPa was detected. In the Ellipticity analysis, the borehole deformation is investigated using Acoustic televiewer data (ATV). An elliptical fitting on the borehole shape allowed inferring a continuous stress orientation profile along the boreholes. Hence, a maximum stress orientation of 77° $\pm$ 29°N was measured along the short boreholes and 151° $\pm$ 23°N along the long borehole.

Significant spatial intra- and inter-borehole variations of the prevailing local in-situ stress were observed. Natural and induced fractures and fault zones reveal to decrease and locally rotate the in-situ stress. Further, a significant influence of tunnel-induced effects on the stress along the boreholes was observed up to a distance of 4 times the tunnel diameter.

Compared to previous stress measurements, the combination of the two chosen methods allows a profound description of the stress distribution and anomalies in the underground of the Bedretto tunnel. This leads to extended understanding of fault reactivation, tunnel-induced effects, in-situ stress variability from local heterogeneities and fracture behaviour inside the crystalline underground.

Acknowledgement

All this work is only possible because of the enormous support of many people involved in the background. Big thanks to Xiaodong as the main supervisor for all the patient mentoring and for leading me through the fascinating field of Geomechanics. Many thanks to Kai for all the codes I could generously use and all the competent help. Many thanks also to Shihuai for the codes, explanations and contributions that have been a fundamental part of this thesis. Thanks also to Marian for the exciting discussions and good input. Many thanks to Quinn, Daniel, Alexis, and the Bedretto team for the support and giving me the chance to contribute as part of the influential Fault Activation and Earthquake Rupture (*FEAR*) and Stress Profiling in Enhanced Geothermal Systems (*SPINE*) projects. Thanks also to Uni Lausanne for acquiring and providing the logging data. Thanks also to my friends and family who supported me understandingly during this process.

Special thanks to Swiss Association of Energy Geoscientists (SASEG), whose support made this work possible at all. Also, thanks to ALT for generously providing WellCAD, which made the work much smoother.

Thank you!

Deborah Stadler, 30.11.2022, Zürich

Contents

List of Figures

List of Tables

Chapter 1

Introduction

Society's desire for a safe, nuclear-free and CO2-neutral energy supply increases interest in possible alternative solutions to replace nuclear plants or fossil fuels. In 2017, the Swiss population voted for the Federal Energy Strategy 2050, in which renewable energies are supported to have a self-sustaining energy supply over a long-term perspective. As a result, the Swiss Competence Centres for Energy Research (SCCER) was founded to support research and promote knowledge transfer. One objective of the SCCER is to strengthen the use of geothermal energy.

One opportunity could be application of so-called enhanced/engineered geothermal systems (EGS). Typically, low-permeability rock is hydraulically stimulated by increasing permeability through hydraulic shearing (HS) of preexisting fractures or hydraulic fracturing (HF) of intact rock. Improving permeability over large-scale leads to higher flow rates and the possibility of water heating or CO_2 storage, whereby electricity generation could be possible. Seismic activity induced by hydraulic stimulation must be clearly understood to ensure the safety of society.

Description of complex hydro-seismo-mechanical activities in underground laboratories of hectometer-scale is necessary to link knowledge from laboratory to reservoir scale. Upscaling and establishing underground laboratories with comparable characteristics are crucial to evaluate potential applications (Gischig et al., 2020). Thus, ETH Zurich created with the Bedretto Underground Laboratory for Geoenergies (BedrettoLab or BULGG) a possibility to conduct relevant experiments in the crystalline underground of the Swiss alps. The aim is to answer open research questions regarding hydraulic stimulation and other complex underground processes, such as fault reactivation, stress heterogeneities, and the influence of fractures and faults on the surrounding rock. This Master thesis attempts to expand knowledge on complex processes of the in-situ stress state of the underground by mapping different boreholes. The stress state is a key factor in determining fracture initiation and propagation. Its understanding and measuring is a fundamental aspect in major applications such as tectonic processes, earthquakes, nuclear waste disposal, underground stability analysis (tunnel, cavern, shaft), as well as the establishment of oil and gas reservoirs.

1.1 In-situ stress

Existing stress can be described by the stress tensor containing components to represent the acting force. From the stress tensor the three principal stresses can be described, which act orthogonally to each other ($S_1 \geq S_2 \geq S_3$), corresponding to the greatest, intermediate, and least principal stress depending on their magnitude. Often the assumption is made that one principal stress is normal to the earth's surface representing the acting overburden and described as S_v, hence it follows that the other two principal stresses act in horizontal direction represented by the maximum horizontal stress S_{Hmax} and minimum horizontal stress S_{hmin} (Zoback, 2007). Based on this concept Anderson (1905) linked the relative stress magnitudes S_{Hmax}, S_{hmin} and S_v to the

principal stresses S_1, S_2 and S_3 predict the local faulting regime (Table 1.1).

Table 1.1: Classification of the fault regime by Anderson's Theory of Faulting

Regime	Stress		
	S_1	S_2	S_3
Normal	S_v	S_{Hmax}	Sh_{min}
Strike-slip	S_{Hmax}	S_v	Sh_{min}
Reverse	S_{Hmax}	Sh_{min}	S_v

The drilling of a borehole in the underground leads to a redistribution of the surrounding in-situ stress state. The resulting new free surface at the borehole wall causes the stress to bend around the borehole (Kirsch, 1898). Subsequently, the compressive stress increases in the direction of S_{hmin} and decreases in the direction of S_{Hmax} (Figure 1.1). If the stress exceeds the rock strength, rock failure (breakouts) occur in the direction of S_{hmin} at the point of the highest stress concentration. On the contrary, tensile failure occurs as a result of the effective minimum principal stress exceeding the tensile rock strength. Tensile fractures align in the direction of S_{Hmax} (Zoback, 2007). Further, anisotropic-acting stress can lead to a deformation of the initial circular-shaped borehole. The elastically deformed borehole can be simplified and displayed by an ellipse-like borehole wall geometry. The Ellipticity analysis (Section 4) uses the geometry of the ellipse to infer the initial stress orientation and give an additional indication of the relative stress magnitude.

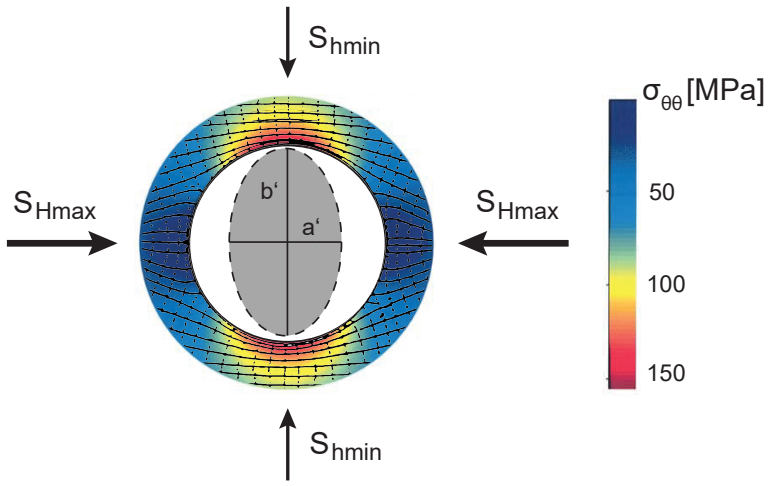

Figure 1.1: Illustration of the acting hoop stress with the bending of the stress trajectories around the borehole, based on Kirsch (1898). Marked are the principal stress trajectories, assuming a vertical-acting principal stress. Resulting in borehole deformations into a simplified ellipse-like shape. Where a' and b' represent the ellipses short resp. long axes. Modified from Zoback (2007); Zoback et al. (2003)

1.2 In-situ stress measurements

Rock in-situ stress can be estimated in the borehole using various measurement methods. A common approach is the use of hydraulic methods. Thereby, an interval is hydraulically isolated and pressurised by injecting water. Based on the pressure response, the stress can be inferred. A separation can be made between the hydraulic fracturing method (HF) and hydraulic fracturing of pre-existing fracture (HFPF) (Hubbert and Willis, 1957; Cornet and Valette, 1984; Haimson and Cornet, 2003). HF is carried out in an intact rock interval, whereby the experiment induces new tensile fractures. HF performed in low permeable rock with a small-scale injection volume is often referred to as Mini-frac tests. In HFPF, on the other hand, interval pressurisation is done on a

pre-existing fracture.

Further fracture-based possibilities for stress estimation are borehole breakouts and dry fracture opening tests (Bell and Gough, 1979; Stephansson, 1983). Other possibilities for stress estimation are relaxation (stress relief) during coring, crack-induced strain relief in drill cores, and combining logging stress with rock properties, as well as physical fault zone properties and their related earthquakes. An overview of the various in-situ stress measurement possibilities is given in Zang and Stephansson (2010).

1.3 Objective

Within the scope of this Master Thesis, the in-situ stress of three boreholes in the BedrettoLab is analysed and investigated to gain a deeper understanding of the local in-situ stress. The two complementing methods, Mini-frac tests and the Ellipticity analysis, are applied. While Mini-frac tests are a widely used method for stress determination (Hubbert and Willis, 1957; Schmitt and Haimson, 2017), the Ellipticity analysis using ATV data is still less established and rarely investigated in scientific publications (Chong, 2021). This work helps to enhance the knowledge and implementation of the Ellipticity method.

A major focus is on the integration of the different methods and techniques. Combining these two different methods enhances the knowledge of increased overall perception and understanding of the regional and local stress field from complementing perspectives. Further, this work aims to contribute to a broader understanding of hydraulic stimulation in the bedrock, rock failure, fault reactivation, stress heterogeneities and their interaction with natural fractures and fault zones of the surrounding bedrock.

This Master thesis is structured in different parts: Chapter 2 contains the characterisation of the study area and the investigated boreholes. In chapter 3 the analysis of the Mini-frac tests is presented. Chapter 4 focuses on the Ellipticity analysis and finally chapter 5 provides a conclusion and outlook of the thesis.

The analysis of the methods refers to three inclined boreholes. However, it also tries to integrate it into the broader context with the help of other already existing boreholes and stress measurements, which have been studied before (Bröker, 2019; Rousopoulou, 2020; Bröker and Ma, 2022; van Limborgh, 2020). Two already existing boreholes were analysed and interpreted, as well as one new-built borehole in the north-west of the tunnel within the framework of the scientific research project *FEAR*. While the stress state and geological structures at the surface, along the tunnel and at boreholes in the south-east direction are well explored and documented (Ma et al., 2022; David et al., 2020), the local stress state in the north-west tunnel direction is little known yet.

Chapter 2

Site characterisation and test boreholes

Using boreholes, various experiments can be conducted to accurately describe the in-situ stress better and understand better geological processes in the underground. Characterisation of the geological and geomechanical features of a borehole and tunnel is a substantial part of the work.

2.1 BedrettoLab and regional geology

The mostly unsupported Bedretto tunnel has a length of 5218 m and connects the Furka Base Tunnel with Bedretto (Ticino). The BedrettoLab is located inside the Bedretto tunnel in the Gotthard massif of the Swiss alps (Figure 2.1a). It operates as a joint underground research facility between the Department of Earth Science at ETH Zurich and the Swiss Competence Center for Energy Research (SCCER). Initially planned as a logistical muck transport from the Furka Base tunnel, the horseshoe-formed Bedretto tunnel has been constructed with the drill and blasting technique. The southern entrance is located at the height of 1480.5 m.a.s.l, with the tunnel axis oriented in NW-SE direction (317°N) and has a slight slope increase of 0.5% towards the north. Distances inside the tunnel are mainly described using the convention Tunnel Meter (TM). Hereby, the southern entrance corresponds to zero. The local coordinate system used for the model refers to the origin in the BedrettoLab niche at TM 2000. The overburden above the Bedretto tunnel is successively increasing to a maximum of 1650 m directly below Pizzo Rotondo (TM 3100).

Geologically, the targeted study area in the Bedretto tunnel is located within the homogeneous massive light grey Variscan Rotondo granite. Paragneiss, Amphibolites and Tremola series are located towards the south and are affected by a landslide with flexural toppling ("Hakenwurf") (Figure 2.1b). The Rotondo granite has intruded into the Gotthard massif during the late Variscan orogeny (Lützenkirchen and Loew, 2011).

The major fault zones are preferentially oriented with a sub-vertical dip and striking in NE-SW to E-W direction. Additionally, numerous brittle fracture structures ranging in the scale of metres occur spatially clustered in the tunnel. The prevailing fractures and at the surface can be simplified into four different sets (dip/dip direction): Tunnel perpendicular set (75°/324°N), E-W striking set (67°/001°N), N-S striking set (79°/271°N) and a tunnel parallel set (84°/220°N) (Jordan, 2019).

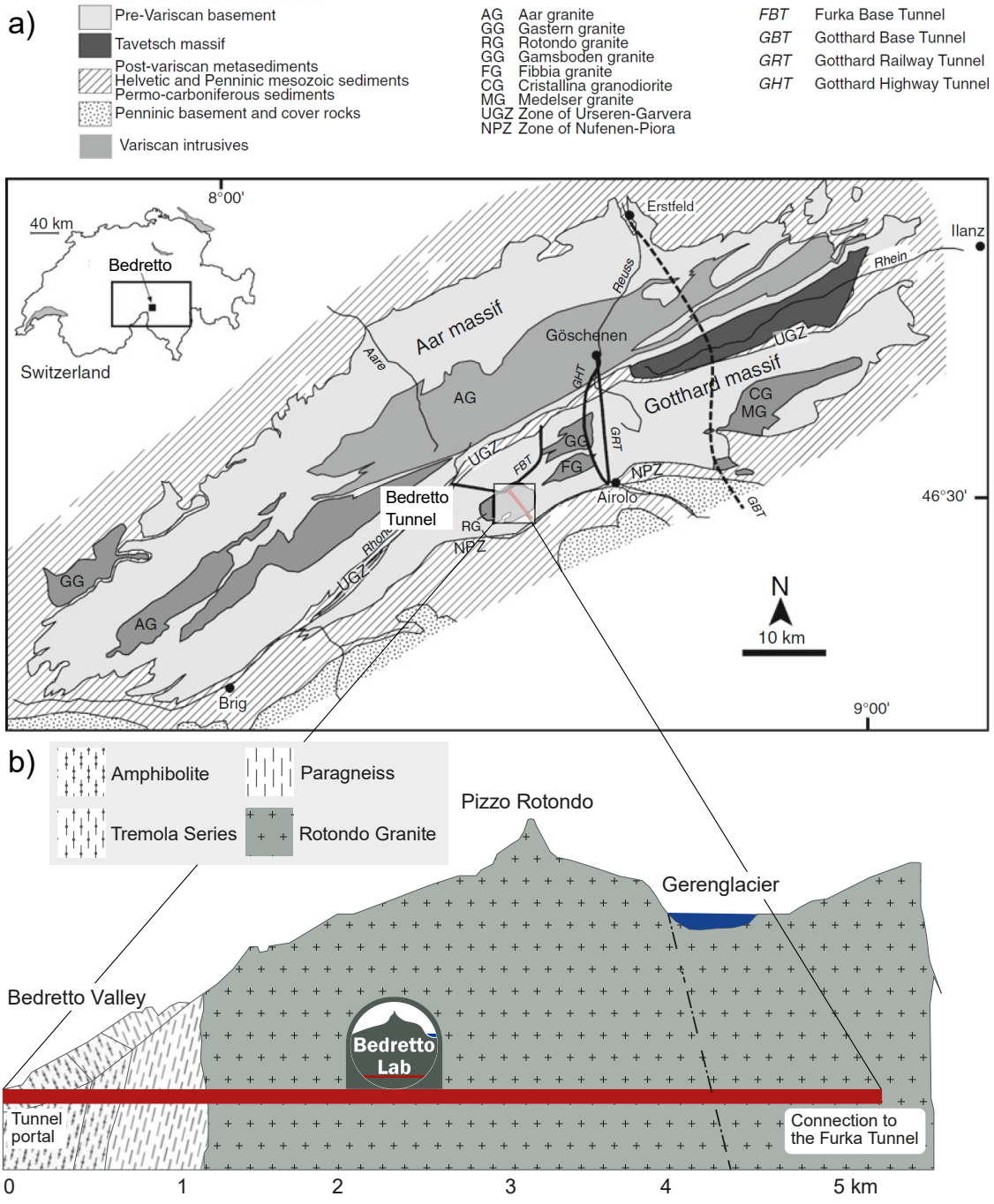

Figure 2.1: **a)** Geological and geographical map from the Aar and Gotthard massiv (adapted from Lützenkirchen and Loew (2011)). **b)** Geological cross-section view of the Bedretto tunnel with the BULGG (Maps, ©BedrettoLab at ETH Zurich, 2020 adapted from Keller and Schneider (1982).

2.2 In-situ stress state

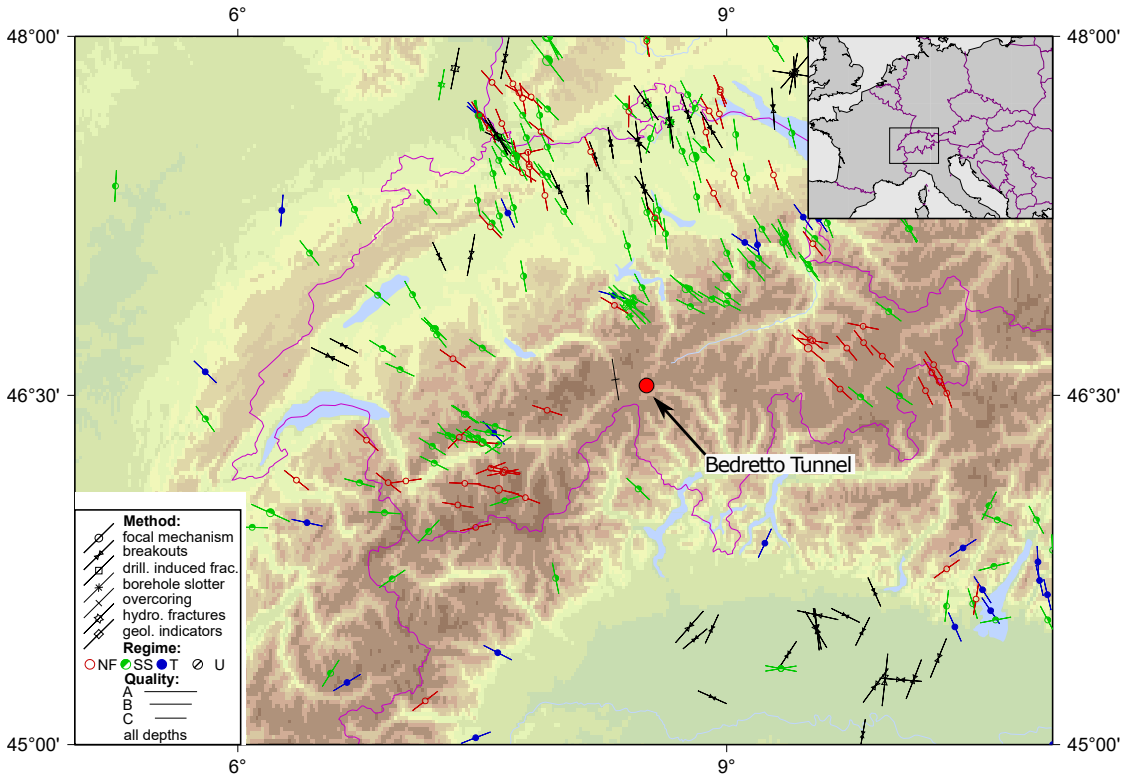

Figure 2.2: Overview of the far-field stress state situation (Heidbach et al., 2016). The map shows the different stress regimes around the Bedretto tunnel from validated stress measurements.

Alpine orogeny predominantly embosses the regional stress field. The World stress map (Heidbach et al., 2016) gives a first impression of the prevailing far-field stress situation (Figure 2.2). Unfortunately, it lacks sufficient data in the region of the study area. The overview gives a rough indication that the azimuth of the acting maximum horizontal principal stress S_{Hmax} is oriented towards the SE quadrant.

Stress-induced failures such as spalling along the sidewalls of the Bedretto tunnel Meier (2017) indicate a horizontal minimum principal stress ($S_3 = S_{hmin}$). Thus, a local reverse faulting regime ($S_3 = S_v$) is unlikely. The Bedretto tunnel reveals a normal faulting regime ($S_1 = S_v$) or a strike-slip regime ($S_2 = S_v$). Ma et al. (2022); Bröker (2019) shows results from Mini-frac tests that indicate the transitional position of the BULGG between normal and a strike-slip fault regime ($S_v \geq S_{Hmax} \geq S_{hmin}$).

The in Bröker and Ma (2022) conducted Mini-frac tests in the SB boreholes (TM 1750 to 2250) reveal a maximum horizontal stress (S_{Hmax}) direction of 100 - 110°N with a magnitude of 25.4 ± 2.3 MPa. The resulting S_3 stress magnitude has been determined at 14.6 ± 1.4 MPa. Additionally, a local pore pressure (Pp) of 2.0 - 5.6 MPa has been measured. The average vertical stress Sv is calculated to be 26.5 MPa (assuming an overburden of 1000 - 1050 m, with a constant rock density of 2.62 $\frac{g}{cm^3}$ from David et al. (2020)). According to Meier (2017), the topographic influence on the stress orientation decreases with higher overburden towards the north, thus suggesting that the orientation of a principal stress becomes vertical from about TM 1500. In-situ stress measurements performed by Bröker and Ma (2022) are in line with other analyses done in the Bedretto tunnel (Ma et al., 2019; van Limborgh, 2020; Bröker, 2019; Rousopoulou, 2020; Chong, 2021).

2.3 Boreholes and measurement campaign

For a large number of experimental projects, several boreholes have been drilled inside the Bedretto tunnel. Within this study, three inclined boreholes have been selected (Table 2.1 and Figure 2.4a). SB 2.2 and SB 2.3 are located in the BedrettoLab niche (Figure 2.4c) and have been built in the first drilling campaign in 2019. The third borehole (BFE_A_05) is located further towards the north (Figure 2.4b) and has been drilled in 2022 as a part of the *FEAR* project.

After the drilling, several boreholes were logged using geophysical logging tools: Acoustic televiewer (ATV) and optical televiewer (OTV). From the derived logs, the boreholes can be geologically characterised. By analysing the logs, it is possible to identify and characterise natural and induced fractures, fault zones and specify the geological rock volume. Logs of the investigated boreholes are attached in the digital Appendix.

Table 2.1: Overview of the borehole properties of the investigated boreholes.
*Azimuth is referred to the magnetic north direction.

Borehole	Position [TM]	Inclination [°]	Azimuth [°N]*	Length [m]	Diameter [mm]	Casing depth [m]
SB 2.2	2075	60	226.9	40	101	1.5
SB 2.3	2095	70	133.9	40	101	1.5
BFE_A_05	2363	30	30.5	216.5	96	7.5

In SB 2.2 and SB 2.3, Mini-frac tests were carried out in different interval depths to characterise the prevailing in-situ stress. Later, the borehole was re-logged using the ATV and OTV tool to document any experiment-induced changes. Figure 2.3 gives a chronological overview of the logging and experiments done in SB 2.2 and SB 2.3. The ATV and OTV logging of BFE_A_05 was done on the 07. September 2022. Various stress determination experiments are prospectively planned for BFE_A_05.

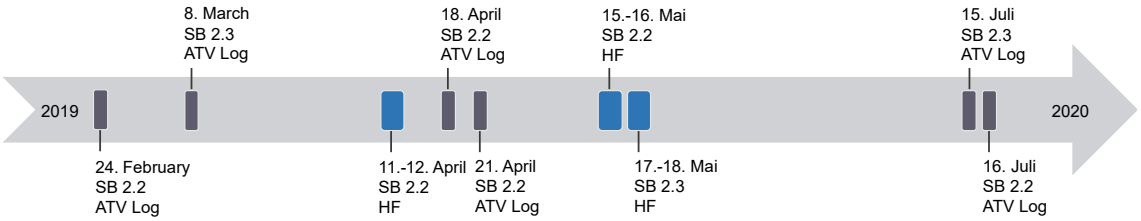

Figure 2.3: Timeline of the ATV logging and hydraulic fracturing experiments of the SB2.2 and 2.3 boreholes. Coloured in grey mark the ATV logging of the borehole, while the blue colour represents the hydraulic fracturing experiments.

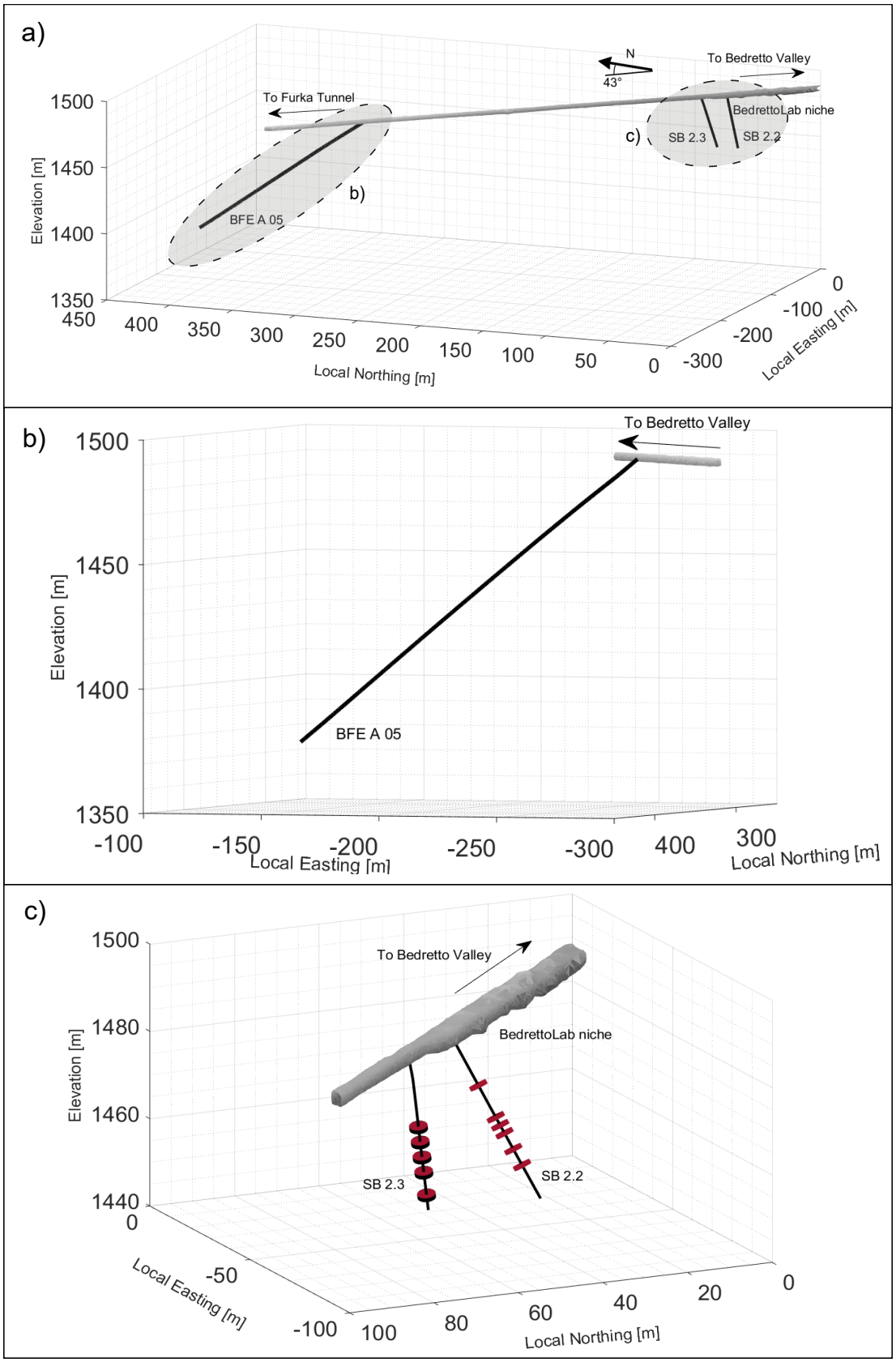

Figure 2.4: **a)** Spatial overview of the investigated boreholes SB 2.2, 2.3 and BFE_A_05. **b)** Zoom of the borehole BFE_A_05. **c)** Close-up of the boreholes SB 2.2 and SB 2.3 at the BedrettoLab niche, boreholes include in red the Mini-frac intervals.

2.4 Geological borehole characterisation

Fractures and fault zones lead to a significant impact on the rock volume behaviour. Hence, it is crucial to determine and document such geological key structures in the target area. This has been done using OTV and ATV image tools and confirmed with core photos. Open geological fractures show a clear fracture trace in the OTV and ATV logs.

Geological characterisation of SB 2.2 and SB 2.3 has been completed by Bröker (2019); Rousopoulou (2020). They could identify several deeply dipping natural open and sealed fractures in an otherwise primarily intact granite.

The borehole BFE_A_05 intersects various geological features, such as open and filled fractures, dykes, composition foliation and mylonitic shear zone. Generally, the filled fractures show a darker colourisation with a grain size reduction and quartz and biotite-rich infill. Ductile shear zones show strong foliation to mylonitic structures with darker colourisation due to a high amount of biotite, chlorite, and epidote, alternating with clear open fractures. The ductile shear zones appear prevalent proximal to brittle fracture zones, with deformed fractured granite, agreeing with the geological characterisation from Ma et al. (2022) of nearby boreholes in the Bedretto tunnel. While compositional foliation structures appear to be further away from the strong deformation zones, often in combination with colourisation changes due to mineralogical variations. Occurring quartz and aplitic dykes reveal an aperture in mm to dm scale.

Table 2.2: Statistical overview about the various picked structures in BFE_A_05.

Structure type; Orientation (striking)	Number of fractures	Percentage
Bt-richt	128	29%
Dyke-vein	32	7%
Un-differentiated	148	33%
Open fractures	62	14%
Foliation compositional	36	8%
Shear Zone-mylonite	42	9%
N-S Orientation	29	6%
E-W Orientation	287	64%
Tunnel perpendicular	57	13%
Tunnel parallel	77	17%

In BFE_A_05, no breakout zones have been detected, indicating a rather higher rock strength or lower in-situ stress compared to the surrounding boreholes CB1 and 2 (van Limborgh, 2020). The majority of the geological structures along the boreholes are oriented towards 60°/360°N (dip/dip direction) (Appendix A.1a). Subsequently, most structures strike E-W (Table 4.1 and Appendix A.1b) and only a minority of the structure planes dip towards 60°/300°N and 81°/223°N. The different oriented fracture sets occur in a clustered behaviour. The dominant E-W striking fracture set occurs predominantly in the proximity of the key fault zones (Figure 2.5).

The borehole reveals three key fault zones, with open fracture structures at a measured borehole depth of 37 m to 46 m, 174 m to 179 m and 193 m to 195 m. The fault zones reveal intense rock deformation with a large number of structures, especially open fractures. The borehole can be summarised into two characterisation units. The first unit from the borehole top to a depth of 174 m exhibits several rather isolated biotite and quartz-filled fractures, aplitic dykes and features a ductile-brittle fault zone at 37-46 m dipping 69°/360°N. The second unit (174 - 216.5 m) shows strong deformations, characterised by highly foliated mylonitic ductile shear structures, intercepted by brittle fault zones at 174 - 179 m (oriented 48°/034°N) and 193 - 195 m (oriented 49°/004°N).

The darker colourisation of the rock unit indicates a high amount of biotite, chlorite and epidote minerals.

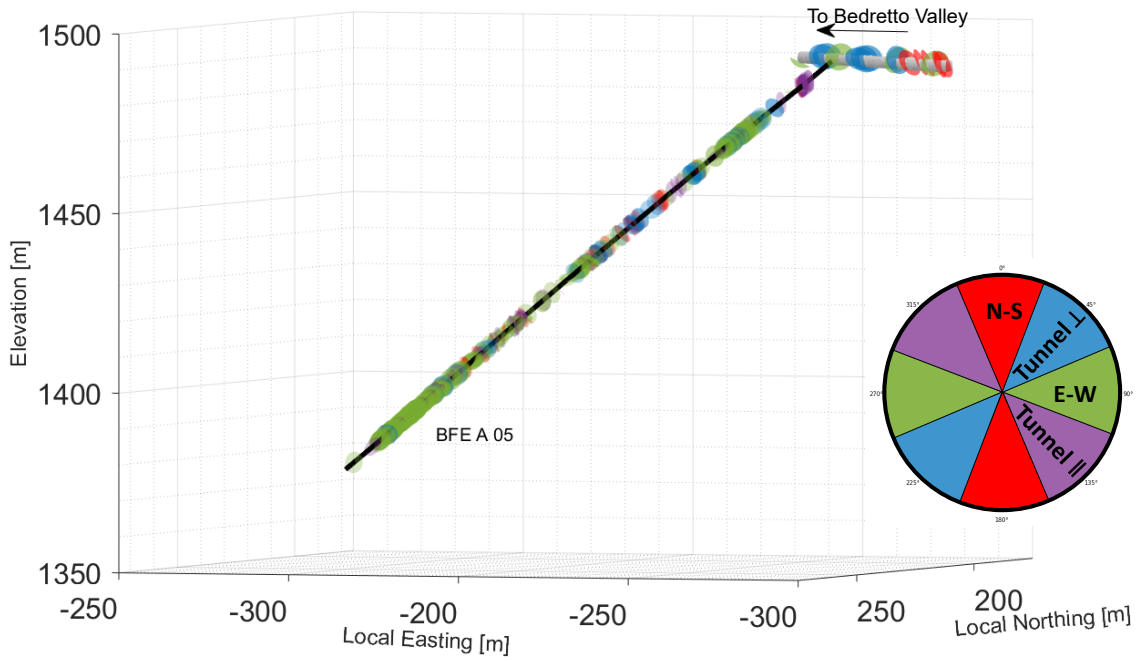

Figure 2.5: Mapped geological structures in borehole BFE_A_05 and along the tunnel (Ma et al., 2022). The classification for the different sets of fractures according to their striking.

Chapter 3

Mini-frac tests

The following chapter presents the analysis of the Mini-frac experiments, which is a diagnostic borehole test to evaluate the minimum principal stress magnitude and its orientation. In this thesis, the focus is on the estimation of the minimum principal stress magnitude from the Mini-frac tests using various methods. As there is no general agreement on the choice of the best method to determine the minimum principal stress magnitude (e.g., McClure et al. (2016); Rutqvist and Stephansson (1996); Schmitt and Haimson (2017). The stress orientation can be determined by analysing the new fracture traces induced by the Mini-frac as shown in Ma et al. (2019); Bröker and Ma (2022). However, this is not the focus of the Mini-frac analysis made in this thesis. The Mini-frac tests have been carried out on the two inclined SB 2.2 and SB 2.3 boreholes. The injection protocols of the conducted Mini-frac tests in the various borehole intervals are attached in the digital Appendix B. The analysis focuses on these boreholes in comparison to other Mini-frac tests within the Bedretto tunnel (Chapter 3.3).

3.1 Method

The Mini-frac experiments were performed by the company MeSy-Solexperts GmbH with Kevlar-reinforced straddle packer elements. The length of the test-interval is 0.7 m, while each packer has a sealing length of 1m (Figure 3.1).

Beforehand, a geological characterisation was conducted using ATV and OTV data. Based on this, the optimal depth intervals were determined. For the Mini-frac tests, the target intervals were chosen to be as intact as possible without any stress- or drilling-induced damage or natural fractures. Subsequently, the test interval was isolated with two inflatable packer elements (Figure 3.1). In the next step, water is injected into the test interval at a constant flow rate, increasing the pressure inside the interval. A similar standard injection protocol is used to that recommended by Haimson and Cornet (2003). At the beginning of the protocol (Figure 3.2), a pulse test is performed for an initial estimate the fracture permeability and to check the functionality of the packers and proper sealing of the interval. Afterwards, the pressure is increased stepwise in the interval until a fracture is initiated and opened. Then in the shut-in phase, the pump is stopped and no fluid is injected or released. Hence, in the bleed-off phase, the interval is vented and the complete hydraulic pressure is released. In three further cycles, the fracture is reopened. Thereby, the fracture propagates further. In the final cycle of the injection protocol, the flow rate is increased stepwise to provide an additional shut-in pressure value and to determine the jacking pressure. An overview of the several intervals with the respecting injected volume conducted in the two boreholes is given in table 3.1. Finally, the borehole wall is mapped after the test to record any induced-hydraulic fracture trace and possible reactivated fracture structures.

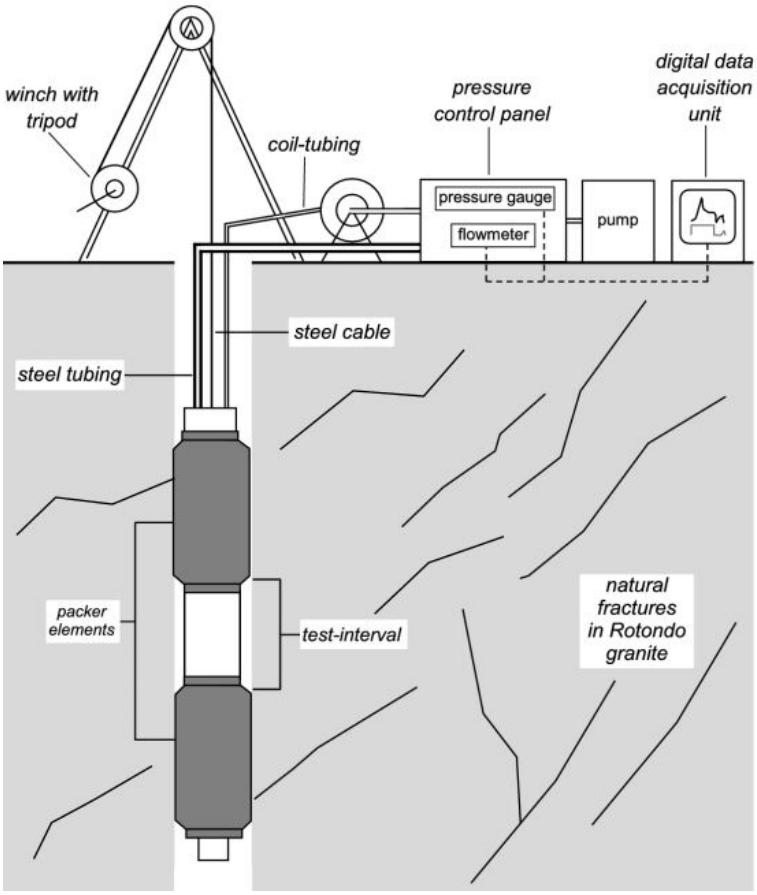

Figure 3.1: Schematic set-up of the Mini-frac equipment. Figure adapted from Bröker and Ma (2022) and Klee et al. (2011).

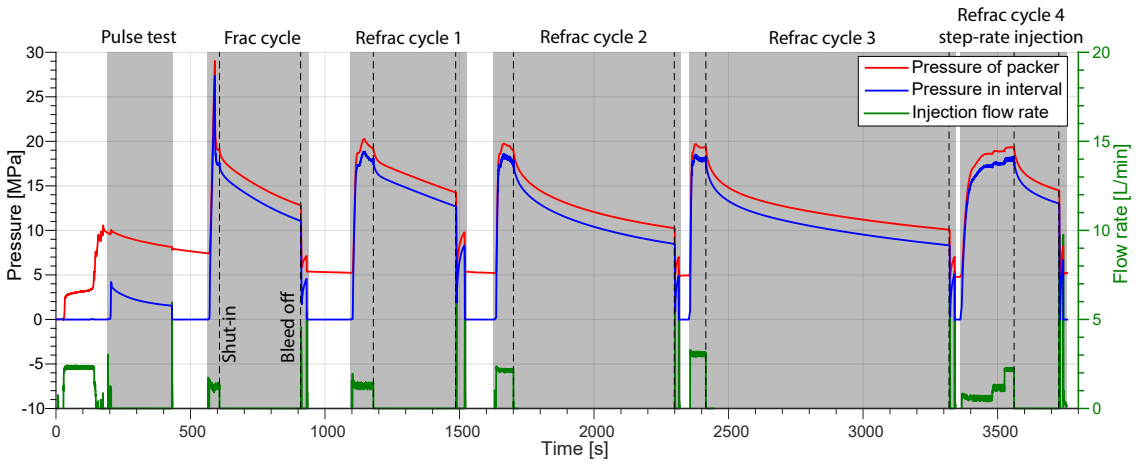

Figure 3.2: Injection protocol of the Mini-frac tests from SB 2.3 in the interval at 30 m. The experiment consists of an initial pulse test and several reopening cycles with a last step-rate injection test. The dotted lines mark the pump shut-in and bleed off.

Table 3.1: Overview of the different depth intervals of the Mini-frac tests performed in SB 2.2 and SB 2.3. The interval depth corresponds to the measured depth of the center of the injected interval.
* No step-rate injection test was done.

Borehole	Interval depth [m]	Injected Volume V_{in} [l]	Numbers of cycles
SB 2.2	11.5	14.0	6
	19.5	8.4	5
	21.5	8.4	3
	23.5	10.7	5
	27.5	10.1	5
	31.5	4.1	4*
SB 2.3	18.0	7.2	4*
	22.0	16.9	5
	26.0	13.7	5
	30.0	11.1	5
	36.0	18.0	5*

With the pressure decay analysis of the pressure response from the Mini-frac test, the following essential pressure parameters can be determined (Figure 3.3):

- Formation breakdown pressure (P_b)
- Instantaneous shut-in pressure (ISIP) (P_{si})
- Fracture closure pressure (P_{cl})
- Fracture reopening pressure (P_r)
- Jacking pressure (P_j)

In the literature (Haimson and Cornet, 2003), the P_{is} is often used as an estimate for S_3. However, it is beneficial to consider and use several methods for a more accurate estimation, allowing a better estimation of the uncertainty range (Bröker, 2019). The following methods were used to estimate S_3 and its uncertainty range: (1) Inflection point $P_{si,inflection}$, (2) Bilinear pressure decay rate on $P_{si,bilinear}$, (3) Fracture compliance method on P_{cl} and (4) jacking pressure P_j.
As proposed in Bredehoeft et al. (1976), the hydraulic tensile strength T_0 can be assessed by the difference between the formation breakdown pressure (P_b) and the fracture reopening pressure (P_r):

$$T_0 = P_b - P_r \tag{3.1}$$

Formation breakdown pressure (P_b)

P_b represents the maximum recorded pressure value of the initial fracture opening cycle. It describes the initiation of the tensile fracture, leading to a sudden increase in fracture volume, resulting in a pressure drop within the test interval.

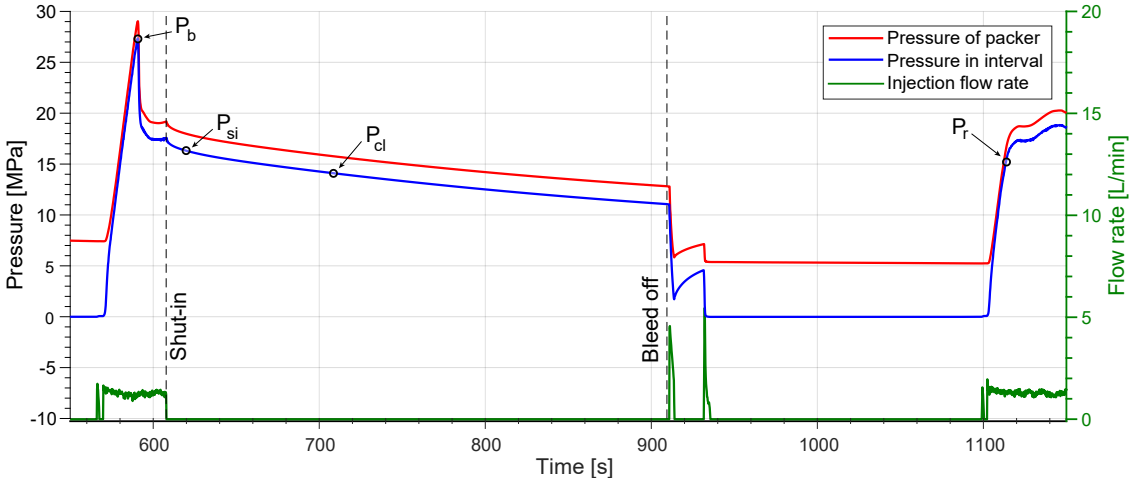

Figure 3.3: Section of the injection protocol SB 2.3 at an interval of 30 m. The cut-out shows the initial breakdown cycle and the first reopening cycle. The various relevant determined pressure values (Formation breakdown pressure P_b, Instantaneous shut-in pressure P_{si}, fracture closure pressure P_{cl} and reopening pressure P_r are marked.

Instantaneous shut-in pressure (ISIP) (P_{si})

This describes the abrupt pressure drop of the instantaneous shut-in pressure P_{si} after the pump is shut-off. This method is widely applied in the industry (Haimson and Cornet, 2003) to estimate S_3. Which then can be determined as follows: (a) Inflection point method and (b) Bilinear decay-rate:

- **(a) Inflection point method**
  Herein, $P_{si,inflection}$ is picked from the deviation of the tangent line after the pump shut off in a Pressure over time (P vs. t plot) (Gronseth and Kry, 1981) (Figure 3.5a). A consistent time window of 30 s was used for all $P_{si,inflection}$ picks.

- **(b) Bilinear pressure decay method**
  In this method, two linear regression curves are fitted manually to the data in a plot pressure derivative versus injection pressure (dP/dt vs. P). The first regression corresponds to the flat, almost horizontal part of the pressure decay curve, while the second regression corresponds to a steep increase of the derivative graph after the shut-in. The intersection of these regression curves yields an estimate of the shut-in pressure $P_{si,bilinear}$ (Lee and Haimson, 1989) (Figure 3.5b).

Fracture closure pressure (P_{cl})

This corresponds to the fluid pressure at the moment when the fracture closes and the walls get mechanically into contact with each other (McClure et al., 2016). Hence, the fracture closing pressure P_{cl} would reasonable approximation to estimate S_3. However, for the small injection volume of the Mini-frac tests, it can be challenging to distinguish between P_{cl} and P_{si} (Schmitt and Haimson, 2017). In addition, in the fracture compliance method, a minimum of the pressure derivative was not always recognisable in the G-Plot. Therefore, a picking could not always be made, leading to fewer available results.

The P_{cl} was determined using the G-function method. The G-function (Nolte, 1979) connects the time-dependent shut-in time with the duration of the fluid injection:

$$G(\Delta t_D, \alpha) = \frac{4}{\pi}[g(\Delta t_D, \alpha) - g(0, \alpha)] \tag{3.2}$$

wherein

$$g(\Delta t_D, \alpha = 1) = \frac{4}{3}[(1 + \Delta t_D)^{1.5} - \Delta t_D^{1.5}] \tag{3.3}$$

α represents the power law exponent for fracture growth, which ranges between the two bounds 0.5 and 1, which is assumed to be 1 (low leak-off or high fluid efficiency), as granite is expected to have very low permeability. While Δt_D represents the dimensionless pumping time, which is defined as $\Delta t_D = \Delta t / t_p$. t_p is the pumping time and is the duration between the injection of the fluid and the pump shut-in, while Δt is the time since the shut-in.

Under ideal conditions, the G-function is linear to the volume of fluid leaked off the fracture after shut-in. In a plot, P vs. G-time, the pressure before fracture closure is therefore expected to be a straight line. At the closure of the fracture, it deviates from the straight line, caused by the increase of fracture stiffness that can be used to estimate P_{cl}. Hence, $P_{cl,compliance}$ is estimated when the pressure derivative increases from the minimum (approx. 10%) (McClure et al., 2014, 2016; McClure, 2022) (Figure 3.5c).

Fracture reopening pressure (P_r)

This corresponds to the pressure required to reopen a previously opened fracture by repressurising the test interval during the reopening cycles. P_r was determined on a pressure plot versus injected plot (P vs. V), where the curve starts to deviate from the linearity, corresponding to a fracture opening displayed by a decrease of the system stiffness (Baumgärtner and Zoback, 1989). This was done by manually fitting a tangent through the curve to determine the location deviation (Figure 3.4).

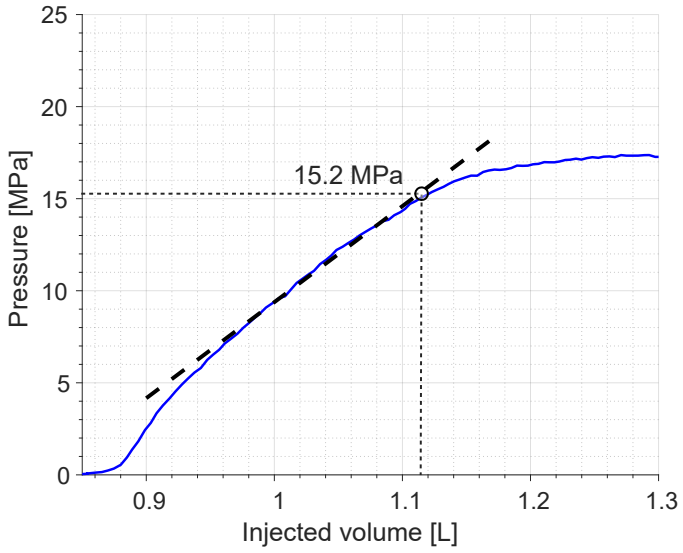

Figure 3.4: Estimation of P_r from the linear pressure trend in the 1st. reopening cycle of SB 2.3 at an interval of 30 m. P_r is determined where the pressure deviates from the linear trend.

Jacking pressure (P_j)

The P_j gives an additional estimate of S_3 from the step-rate injection test (Doe and Korbin, 1987). In the step rate injection, the flow rate inside the interval increases stepwise until the pressure is equilibrated. The P_j was determined on a pressure versus flow rate plot (P vs. Q), in which two linear regression curves are fitted through the different pressure values of the several steps, representing the flow in the closed fracture respective the reopened fracture. By extrapolating the

second flatter regression to 0 l/min flow rate the P_j is measured (Rutqvist and Stephansson, 1996) (Figure 3.5d).

Since the noise of the pump is reflected in the data, and this is expressed in the analysis by the amplification of the derivative, a smoothed average filter was applied for the picking of P_{si} and P_{cl} (e.g., Bröker and Ma (2022)).

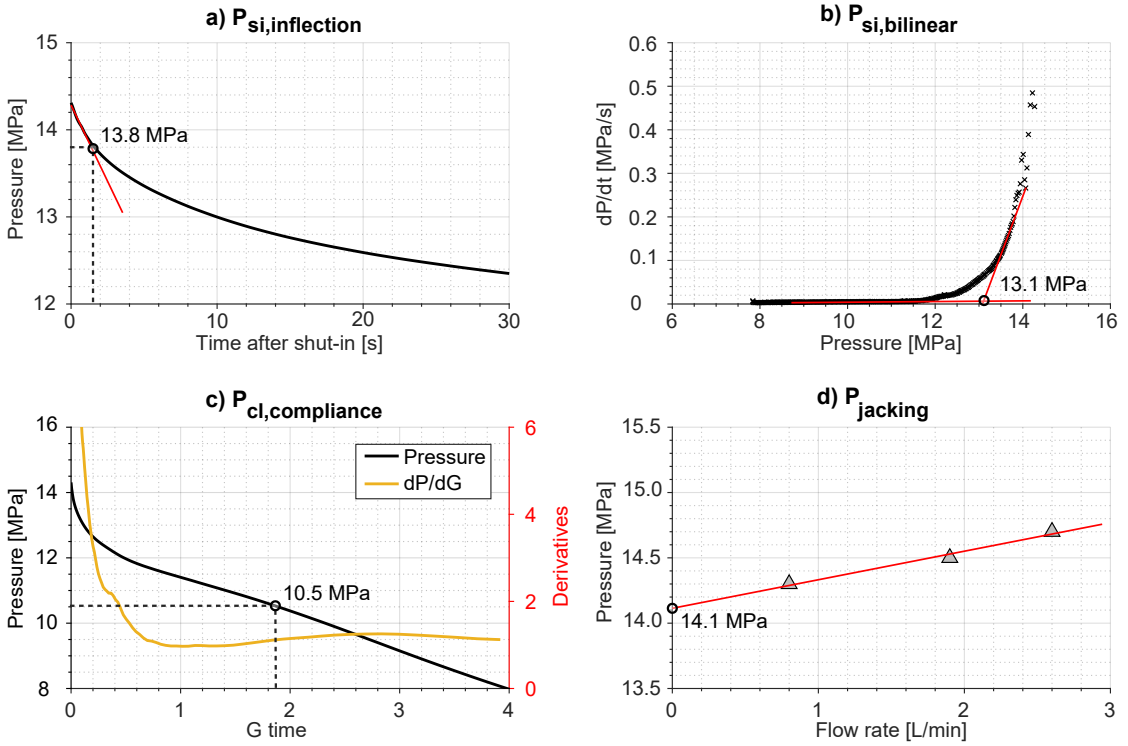

Figure 3.5: Overview of the different picking techniques used to estimate S_3 on the example of SB 2.2 in the interval 23 m of the step-rate injection cycle. **a)** shows the picking of the P_{si}, according to the inflection point method. **b)** illustrates the picking of the P_{si}, according to the bilinear pressure decay method. **c)** example of the fracture compliance method for determining P_{cl}. **d)** Jacking pressure method for the estimation of $P_{jacking}$ out of the step rate injections.)

3.2 Results

The results of the pressure transient analysis from the Mini-frac tests reveal a wide variability along the borehole, within the different injection cycles and between the investigated boreholes. An overview of the pressure results is given in Appendix Table A. The average pressure of each Mini-frac interval was calculated as a mean over all fracture cycles within the specific interval. While the final borehole pressure and its standard deviation was calculated as an average over the averaged interval values.

SB 2.2 shows a $P_{si,inflection}$ of 14.9 ± 2.3 MPa, while the $P_{si,bilinear}$ is slightly lower with 14.1 ± 2.2 MPa. It is evident that the stress magnitude changes in the different interval depths of the borehole (Figure 3.6a). Thus, the $P_{si,inflection}$ in the shallowest interval at 10.5 m (Measured depth) exhibits the highest magnitude with 18.8 ± 0.4 MPa of all determined pressures. Furthermore, the intervals at 19.5 m and 21.5 m show the lowest pressure values in the borehole with $P_{si,inflection}$ of 12.9 ± 0.3 MPa and 12.6 ± 0.3 MPa, respectively. This indicates a pressure drop at these depths. Afterwards, an increase in the pressure values can be observed. With $P_{si,inflection}$ values ranging from 14.2 ± 0.1 MPa, 14.7 ± 0.5 MPa to 16.1 ± 0.6 MPa in the interval depths

23.5 m, 27.5 m and 31.5 m, the measured pressure values continue to increase with depth. The magnitude trend of $P_{si,inflection}$ is characteristic also for the other determined pressures P_b, P_r, $P_{si,bilinear}$ and $P_{cl,compliance}$, these all show a similar magnitude trend with borehole depth. The two overnight shut-ins lead to a P_p of 2.5 MPa and 3.1 MPa at a depth of 11.5 and 31.5 m, which reflects an increase of the P_p with depth. The magnitude variation of the pressure values along the depth of the borehole is higher than the standard deviation, indicating that the stress conditions change along the borehole.

In borehole SB 2.3, a similar stress behaviour is recognisable. Over the total borehole, the $P_{si,inflection}$ is 16.3 ± 3.3 MPa and the $P_{si,bilinear}$ smaller with 15 ± 3 MPa. A change of stress magnitude along the various interval depths is visible (Figure 3.6b). The most shallow interval at 18 m depth shows a high magnitude $P_{si,inflection}$ of 19.3 ± 0.5 MPa. In the interval at 22 m, the $P_{si,inflection}$ is with 12.1 ± 0.9 MPa, revealing the lowest value over the entire borehole. This suggests a pressure drop around that depth. After that, $P_{si,inflection}$ exhibits an increase with depth, so $P_{si,inflection}$ is increasing in the intervals 26 m, 30 m and 36 m with 13.5 ± 0.3 MPa, 17.3 ± 0.1 MPa and 19.3 ± 0.3 MPa. The other pressures P_b, P_r, $P_{si,bilinear}$ and $P_{cl,compliance}$ again show a similar pressure profile along the borehole confirming the pressure drop at a depth of 22 m. Two overnight shut-ins were performed, resulting in two pore pressure values (2.7 MPa and 3.7 MPa at 18 m and 36 m depth, respectively), indicating an increase in pore pressure with depth. The variation in magnitude of the pressure along the depth of the borehole is greater than the standard deviation, suggesting likewise to SB 2.2 that the stress conditions along the borehole vary.

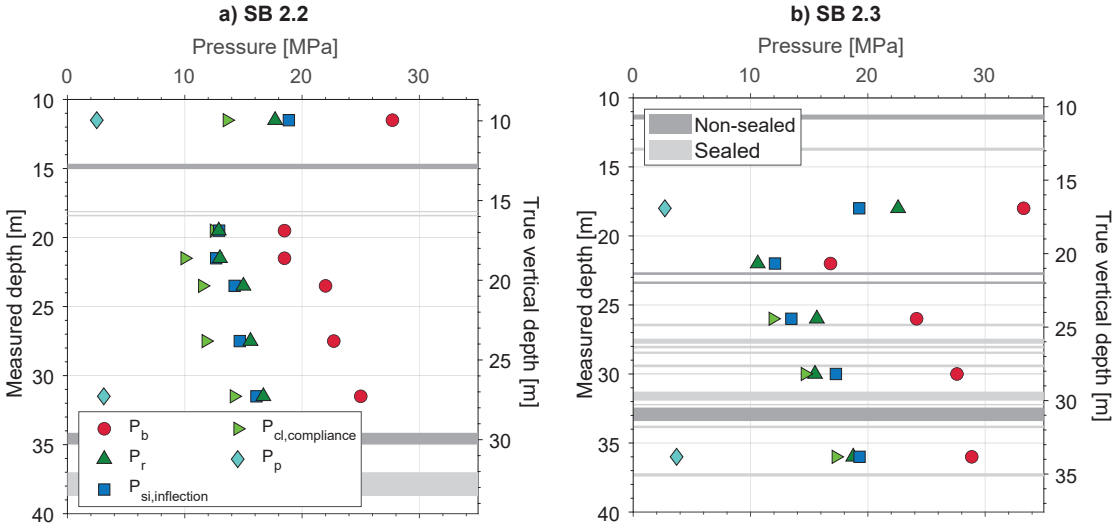

Figure 3.6: Mini-frac results of the investigated boreholes **a)** SB 2.2 and **b)** SB 2.3. The various determined mean pressures are displayed along the borehole: Formation breakdown pressure P_b, reopening pressure P_r, Instantaneous shut-in pressure from inflection point method $P_{si,inflection}$, fracture closure pressure from compliance method $P_{cl,compliance}$ and pore pressure from the overnight shut-ins P_p. The figures represent the mean pressure without its corresponding standard deviation.

The fracture compliance method to assess the P_{cl} was found to be challenging. Concretely, local minimum in the pressure derivative were not always recognisable, as either the shut-in was too short or, in some cases, no increase was recognisable (more on this in section 3.3). Consequently, in borehole SB 2.3, no values were measured in the intervals 11m, 18 m and 22 m and in borehole SB 2.2, only one value was measured in the intervals 19.5 m and 21.5 m, whereby in these intervals no standard deviation is provided. Furthermore, in borehole SB 2.2 intervals 31.5 m and SB 2.3 intervals 18 m and 36 m, no step-rate injection was performed, thus, no results of $P_{jacking}$ can be obtained. In borehole SB 2.3 interval 22 m, only two steps were carried out, so a regression

through the two steps is not meaningful and hence not included.

The investigated P_b in SB 2.2 and SB 2.3 is between 16.8 - 33.3 MPa (mean 24.2 ± 5.0 MPa). The measured values of P_r are 10.6 - 22.6 MPa (mean 15.9 ± 3.2 MPa). In general, P_r is in the same range of values (<1.5 MPa) as $P_{si,inflection}$. An increase of the P_p with depth was observed on both short boreholes from 2.5 to 3.7 MPa. The tensile strength (T) is calculated from the difference between P_b and P_r (equation 3.1), where T was computed to be between 5.5 - 12.1 MPa (mean 8.3 ± 2.2 MPa).

To give a estimate for S_3 four different pressure parameters ($P_{si,inflection}$, $P_{si,bilinear}$, $P_{cl,compliance}$ and $P_{jacking}$) were determined to estimate S_3 in the borehole SB 2.2 (Figure 3.7a) and SB 2.3 (Figure 3.7b). The instantaneous shut-in pressure (P_{si}) was determined using the inflection point method ($P_{si,inflection}$) and the bilinear pressure decay method ($P_{si,bilinear}$). In the investigated boreholes, the $P_{si,inflection}$ method gives an average higher estimate of 1 MPa of the shut-in pressure than the bilinear pressure decay method. The values with the inflection point method are between 12.1 to 19.3 MPa (mean 15.6 ± 2.8 MPa), while with the bilinear pressure decay method, the values range between 11.3 to 18. 3 MPa (mean 14.4 ± 2.5 MPa). Compared to the other S_3 estimation methods, $P_{cl,compliance}$ exhibits the lowest results, ranging between 10.0 - 17.3 MPa (mean 12.9 ± 2.3 MPa) and are thus mostly about 2.5 MPa lower than $P_{si,inflection}$. With $P_{jacking}$, another method was used to estimate S_3 based on the step-rate injection tests. The determined $P_{jacking}$ parameter varies between 13.1 - 18.3 MPa (mean 15.1 ± 2.0 MPa), hence a similar behaviour was observed as $P_{si,inflection}$ revealing small variations (<1 MPa) over the different intervals.

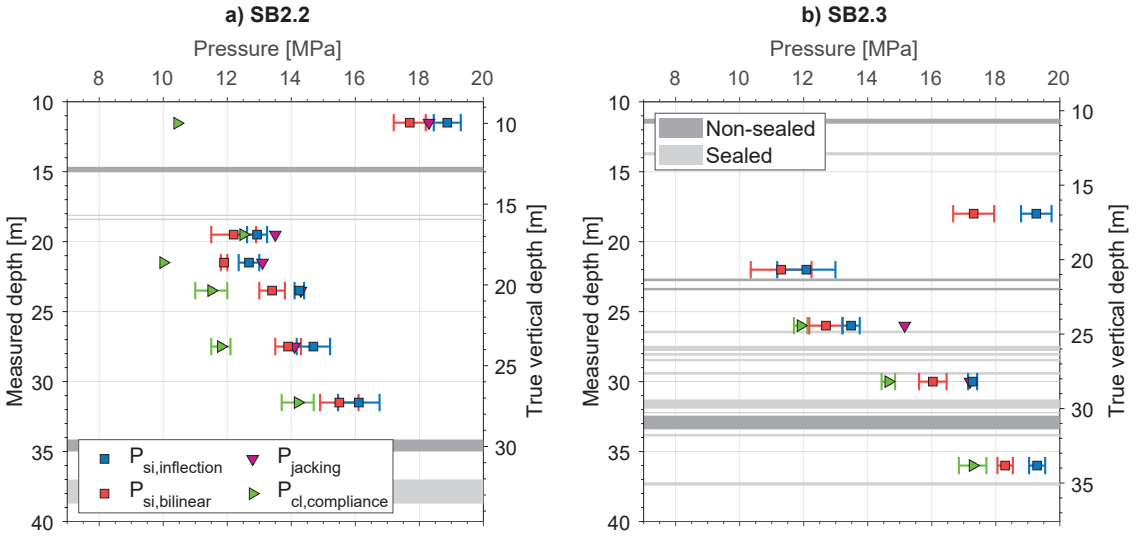

Figure 3.7: The various methods to estimate S_3 from the Mini-frac tests in the investigated boreholes **a)** SB 2.2 and **b)** SB 2.3. The following various determined pressure parameters are shown along the borehole: Instantaneous shut-in pressure using the inflection point method ($P_{si,inflection}$), instantaneous shut-in pressure using the bilinear pressure decay method ($P_{si,bilinear}$), closure pressure using the compliance method ($P_{cl,compliance}$) and Jacking Pressure ($P_{jacking}$). The error bar reflects the standard deviation of the data. If no error bar is shown, only one data point is available.

It is observed that P_{si} reveals variations of 0.5 - 2 MPa between the different injection cycles. P_r tends to decrease over the different injection cycles (0.1 - 3 MPa), as a result of the increase of fracture length and the decrease of fracture stiffness with repeated fracture reopening. Revealing also with advancing reopening cycle where it became more challenging to determine P_r, as the pressure curve shows decreasingly linear behaviour.

3.3 Discussion

Figure 3.8 shows the various pressure parameters determined, combined with the Mini-frac results from the surrounding boreholes (Bröker and Ma, 2022). It reveals that the obtained pressure parameters are consistent among the nearby boreholes. In addition, Bröker (2019) observed an increase in pore pressure with depth, which can be confirmed in SB 2.2 and SB 2.3. However, the obtained pore pressure shows a smaller depth gradient than in the surrounding vertical boreholes. Reduction of the surrounding pore pressure could result from the drainage effect caused by the tunnel. The hydraulic tensile strength (T) calculated from the P_b and P_r ranges from 5.5 - 12.1 MPa (mean 8.3 ± 2.1 MPa), which is consistent with the obtained Mini-frac results of Bröker and Ma (2022). In addition, David et al. (2020) has carried out Brazilian tests on Bedretto granite in the laboratory, measuring a T of 6.78 ± 0.25 MPa, which is in agreement with the observed values.

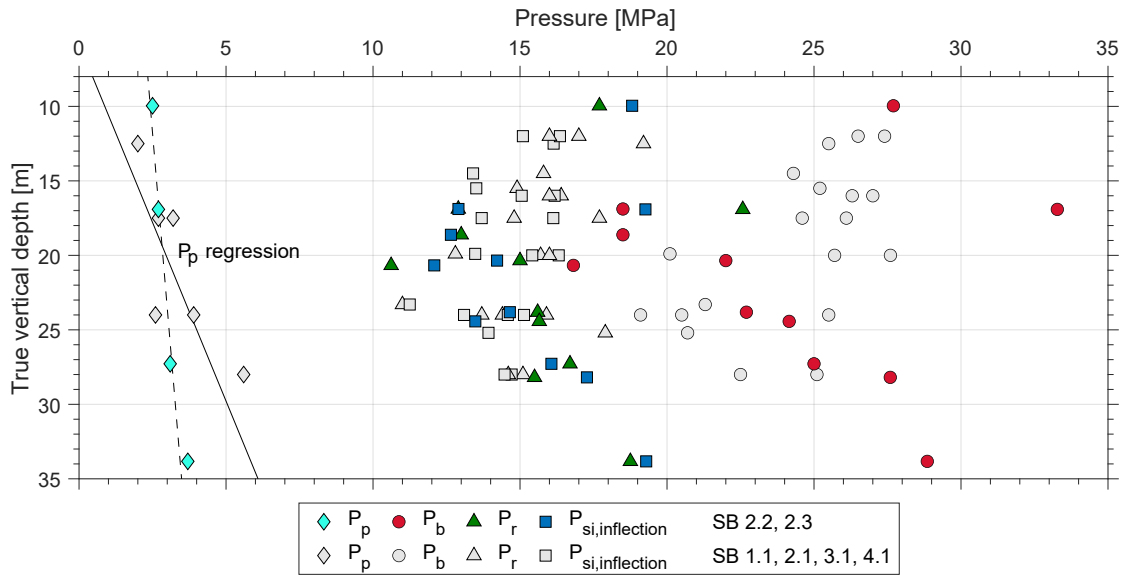

Figure 3.8: Comparison of the determined pressure parameters of the inclined SB 2.2 and SB 2.3 (colored) boreholes to the surrounding vertical SB 1.1, 2.1, 3.1 and 4.1 boreholes (grey) identified and described in Bröker and Ma (2022). The solid linear regression includes all SB values, while the dashed regression includes only the investigated boreholes SB 2.2 and SB 2.3 of this study.

Various methods were applied in order to estimate S_3: (1) Inflection point method $P_{si,inflection}$, (2) Bilinear pressure decay method $P_{si,bilinear}$, (3) compliance method on P_{cl} and (4) $P_{jacking}$. The methods display a similar magnitude profile along the analysed boreholes. However, within the different borehole intervals, the various methods reveal magnitude variations up to 3 MPa in most cases. Combining boreholes SB 2.2 and SB 2.3, $P_{cl,compliance}$ presents the lowest magnitude (12.9 ± 2.3 MPa), while $P_{si,inflection}$ presents the highest magnitude (15.6 ± 2.8 MPa). Whereas $P_{si,bilinear}$ (14.4 ± 2.5 MPa) and $P_{jacking}$ (15.1 ± 2.0 MPa) lead to a slight smaller magnitude. P_{si} reflects the required pressure to keep the fracture open after shut-in. Which is inherently higher than P_{cl}, describing the pressure where the fracture closes again. In a Mini-frac analysis of the surrounding SB boreholes Bröker and Ma (2022) obtains comparable results and findings ($P_{si,inflection}$: 14.6 ± 1.4 MPa, $P_{jacking}$: 14.8 ± 1.5 MPa, $P_{si,bilinear}$: 13.8 ± 1.6 MPa and $P_{cl,compliance}$: 12.9 ± 2.1 MPa) (Figure 3.9). However, it should be noted that the from Bröker and Ma (2022) studied boreholes are vertical boreholes, and the boreholes investigated within this study are inclined, which may affect the pressure transient analysis as the borehole inclination can affect fracture closure process and water flow.

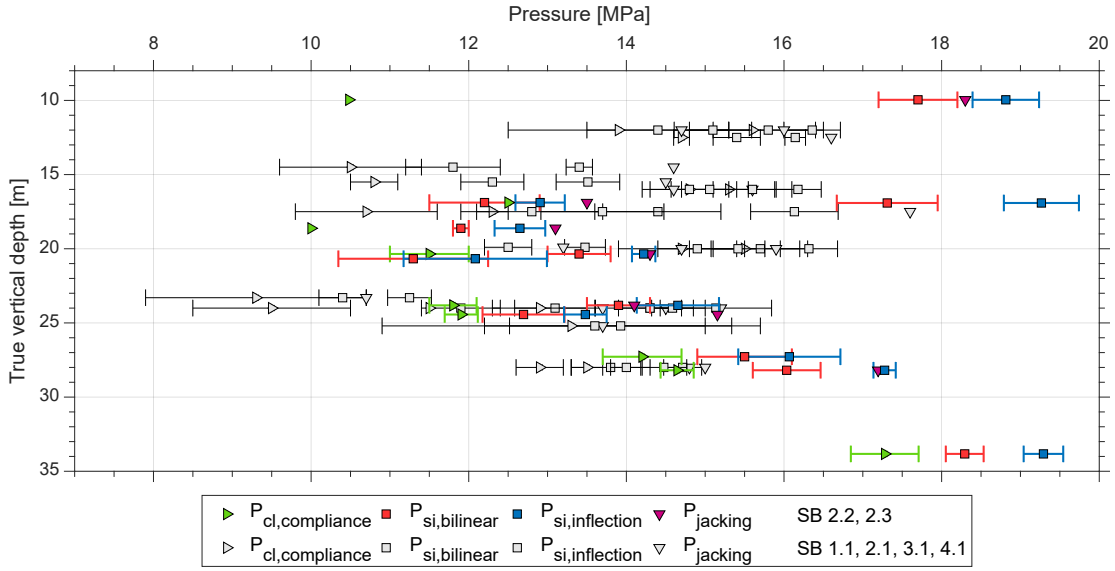

Figure 3.9: Comparison of the S_3 methods in the inclined SB 2.2 and SB 2.3 (colored) boreholes to the surrounding vertical SB 1.1, 2.1, 3.1 and 4.1 boreholes (grey) identified and described in Bröker and Ma (2022). The error bar reflects the standard deviation of the data. If no error bar is shown, only one data point is available.

Spatial stress variation

The boreholes investigated in this work indicate spatial stress variations between the boreholes as well as within the boreholes. In SB 2.2 and SB 2.3, a significant pressure drop was observed at a depth of about 20 - 25 m. In particular, SB 2.3 reveals a significant pressure drop between 18 to 22 m of about 7 - 8 MPa within 4 m distance. This may be caused by heterogeneities in the underground such as natural fractures. For instance, SB 2.3 reveals open fractures at a tunnel depth of 23 m, which could correspond to an in-situ stress reduction. Chang and Jo (2015) could reveal stress variation around natural fractures and fault zones. A tunnel can lead to stress redistribution, drainage effects and temperature cooling, affecting stress conditions around a tunnel. In contrast, Fu et al. (2018) exhibits a reduction of S_3 towards the tunnel due to the temperature effect. However, the analysed boreholes indicate an increase of S_3 towards the tunnel above the observed stress drop at 20 - 25 m depth. Furthermore, the surrounding vertical boreholes do not show a stress drop around 20 - 25 m depth, which argues against the tunnel being a major cause of the prevailing stress variations. However, boreholes SB 2.1 - 2.3 are positioned in the BedrettoLab niche, where the tunnel diameter is larger (6 m) than in boreholes SB 1.1, 3.1 and 4.1 (3 m). Thus the penetration of tunnel-induced stress changes is deeper in the BedrettoLab niche.

Limitations of the method

The determination of the P_{si} has generally proven to be a robust S_3 determination method, as for each injection cycle, both the inflection point and the pressure decay method could be applied. The fitting of the regression curves to determine the $P_{si,bilinear}$ and P_r was done manually, which entails certain inaccuracies. The values were read manually from the plot for all pressure parameters, which proved to be somewhat subjective, leading to uncertainties. $P_{jacking}$ was determined from the step-rate injection. However, this was not carried out for every interval and if so, mostly only three steps were taken, resulting in a lack of data to reliably make two regression curves for the flow of open and closed fracture. Consequently, only one regression was fitted, assuming an open fracture flow for backward extrapolation of $P_{jacking}$ to a flow rate of 0 l/min. The determination of the P_{cl} with the fracture compliance method turned out to be often challenging. On the one hand, a moderate increase of the dP/dG curve results in a somewhat subjective determination of the precise picking point. However, the strong pressure decrease significantly impacts the magnitude

of P_{cl}. McClure (2022) suggested setting the picking of $P_{cl,compliance}$ at an increase from the local minimum of about 10%, however, sometimes the pressure derivative did not increase that much from the local minimum. In addition, fluctuations in pressure from the pump were often observed at the beginning (0-1 G-time) after the shut-in. It was also observed that a local minimum of the pressure derivative is not always recognisable and therefore, the method is not always applicable. Resulting in an $P_{cl,compliance}$ applicability of 47% in the injection cycles. Possible explanations could be a too short shut-in, water injection into or intersecting of a highly conductive natural or pre-existing fracture, where the fracture closure is rapid McClure et al. (2019).

Based on the outcome of the various methods and their limitations, it is recommended to determine the S_3 with P_{si}, estimated reasonably with the inflection point and the bilinear pressure decay method. This agrees with findings from other studies (Bröker and Ma, 2022; Dutler et al., 2020).

Chapter 4

Ellipticity analysis

The stress conditions in the underground act on the borehole, impacting its geometry. Deformations of the borehole can thus be used to infer the in-situ stress distribution of the underground. Heterogeneous stress causes the initial circular-shaped borehole to be deformed. This deformation can be represented by an ellipse-like borehole shape. Thus, analysing the orientation and the axes ratio of the ellipse can provide valuable information about the prevailing in-situ stress condition of the underground.

Inference of the prevailing in-situ stress from the elastic deformation of the borehole has been presented in previous studies. However, the deformation has been chiefly investigated using four-arm caliper logs and poro-visco elastic finite element models (Han et al., 2021), artificial neural network and genetic algorithm (Zhang and Yin, 2014; Zhang et al., 2016; Han and Yin, 2018) or based on the diametrical core deformation (Ziegler and Valley, 2021; Funato et al., 2012).

In this study, the borehole shape was determined using the ATV travel time data. The advantage of this approach is that through borehole economically and rapidly logging, a stress analysis along the complete borehole can be done giving a high vertical resolution. As a result, the orientation of the minimum stress (S_{min}) and maximum stress (S_{max}), their relative magnitude and the stress difference can be determined. This technique is a valuable and a practical complement to further in-situ stress measurements of the underground. However, the approach has been developed recently with only a few scientific publications (e.g., Chong (2021); van Limborgh (2020)).

All results and angles are given with respect to Magnetic North (NM) (Except Appendix Figure A.6). Hence an azimuth of 0° points towards the magnetic north pole. In this analysis, the magnetic declination was not taken into account. ATV data logs of the investigated boreholes are attached in the digital Appendix B.

4.1 Methods

For the Ellipticity analysis, the travel time data of the ATV tool is used. The high-resolution structural logging tool sends ultrasonic waves, which are reflected by the borehole wall and recorded by its receiver. The captured waves provide an amplitude and travel time log that can be used to visualise the borehole wall. These logs are particularly beneficial for geological characterisation (borehole wall roughness and filling of the fractures). Compared to other stress measurement methods, this tool is time and economically efficient, as the logs are usually anyway acquired for the geological description. In addition, as the logging is usually done over the total borehole length, it is possible to describe the inferred stress state along the complete borehole in high resolution.

For logging, the ATV tool QL40-ABI-2G from Advanced Logic Technology (ALT) was used with the ALT Scout data logger and Mount Sopris MXB winch. An overview of the different specifica-

tions of the analysed data sets of the different boreholes is given in Table 4.1.

Table 4.1: Logging details of the ATV logging in the boreholes. In all logging runs, an angular resolution of 1°was applied.
* Data set was not further incorporated due to mechanical issues with the centralizer during the logging.

Borehole	ATV logging dates [dd.mm.yy]	Logging speed [m/min]	Logging depth range [m]	Angular resolution [°]	Depth step [cm]
SB 2.2	24.02.19	0.7	1.67 - 40.10	1	0.19
	18.04.19*	0.7	1.70 - 40.00	1	0.19
	21.04.19	0.7	1.66 - 39.95	1	0.19
	15.07.19	0.9	1.68 - 37.40	1	0.19
SB 2.3	08.03.19	0.7	1.65 - 40.00	1	0.19
	15.07.19	0.9	1.64 - 39.95	1	0.19
BFE_A_05	07.09.22	1.7	2.05 - 216.10	2.5	0.42

The ATV data is imported into the WellCAD software and then further analysed using MATLAB®. Assuming a constant acoustic velocity of the drilling fluid v_a (Water: $1450\frac{m}{s}$) with constant radius of the ATV tool r_p ($9.5mm$). Considering the travel time $\Delta t(\theta, z)$, the borehole radius $r(\theta, z)$ can be consequential calculated:

$$r(\theta, z) = \frac{\Delta t(\theta, z) * v_a}{2} + r_p \tag{4.1}$$

In a standard workflow, ATV data is usually centralised in WellCAD. During this process, the sinusoidal trend is removed (Appendix A.2). In this study, this was not applied to the ATV data to preserve the sinusoidal trends in the borehole shape, which is essential for the elliptical fitting. In addition, an average filter was applied vertically to reduce noise and oscillations, whereby a depth interval of 0.4 m was used for all investigated boreholes (Chong, 2021).

The calculation of the borehole radius $r(\theta, z)$ allows to map the shape of the complete borehole wall over the entire borehole length. As the prevailing in-situ stress has deformed the borehole, this deformed borehole can be represented by an ellipse. With the help of the least square fitting method (Halır and Flusser, 1998), Chong (2021) and van Limborgh (2020) have developed a code that allows to fit an ellipse to the deformed borehole cross-section. From the ellipses short a' and long b' major axes, the orientation of the principal stresses is inferred (Figure 1.1). Applying the ellipse fitting along the depth allows to construct a continuous in-situ stress profile along the entire borehole and therefrom revealing small-scale stress variations.

Further, the ellipticity ratio R can be determined as follows:

$$R = \frac{a'}{b'} \tag{4.2}$$

As the ellipse short axis a' represents the direction of S_{max}, correspondingly vice versa, b' refers to the orientation of S_{min}. Hence, the ellipticity ratio R indicates the relative stress magnitude of S_{max} to S_{min}.

Assuming that the rock is homogeneous, isotropic and deforms elastically. The stress difference can be calculated as follows (Funato et al., 2012):

$$S_{max} - S_{min} = \frac{d_{max} - d_{min}}{d_0} * \frac{E}{1 + v} \tag{4.3}$$

Wherein $S_{max} - S_{min}$ represents the stress difference, as the investigated boreholes in this study are inclined, the stress difference does not correspond to the deviatoric stress. $d_{max} - d_{min}$ corresponds to the difference between the maximum and minimum diameter of the fitted ellipse, d_0 represents the borehole diameter which was simplified to be constant from the drilling. E and v are Young's modulus and the Poisson's ratio, which are assumed to be $E = 45.9 \pm 4.9$ GPa and $v = 0.37 \pm 0.02$ for a water-saturated rotondo granite following (David et al., 2020).

To assess the goodness of the elliptical fitting, the root-mean-squared error (RMS) is calculated from the square root of the squared difference between the real and the fitted ellipse radius.

4.2 Results

It should be taken into account, that the investigated boreholes (SB 2.2, SB 2.3 and BFE_A_05) are inclined. The local orientation of S_{min} and S_{max} differs from the far-field stress orientation and accordingly does not correspond to the horizontal principal stresses S_{hmin} and S_{Hmax}. As a consequence, a forward modelling or a stress inversion is required to make it well comparable with the far-field stress.

Figure 4.1 shows an example of the borehole cross-section and radius, the fitted ellipse and the resulting long axis azimuth of 73°N at a depth of 120 m. Deformations in the borehole cross-section are mostly not recognisable visually but can be recognised graphically as a change of the radius. With the algorithm, the borehole shape is fitted to an ellipse.

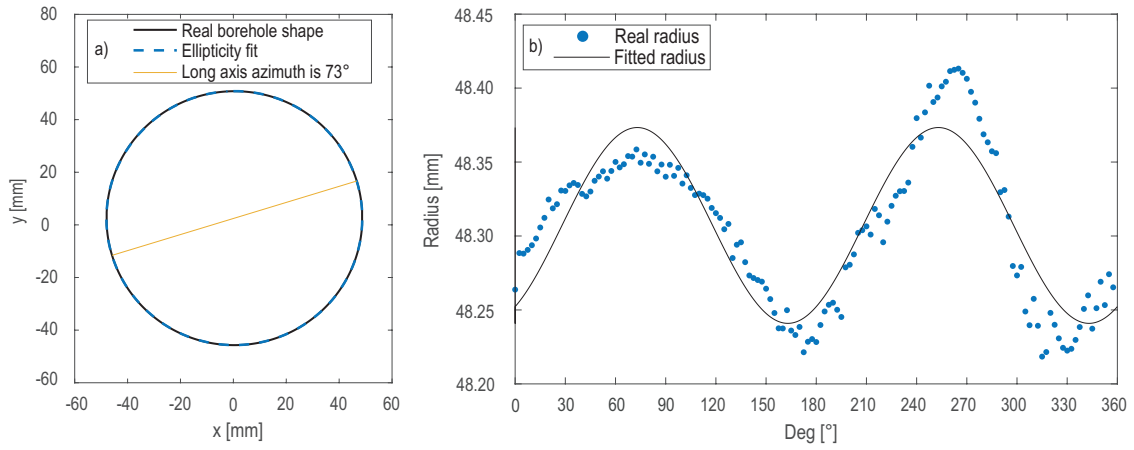

Figure 4.1: Figures of the borehole shape of BFE_A_05 at a depth of 120 m derived by the ATV data. **a)** shape of the borehole, including the fitted ellipse and the long-axis azimuth. **b)** radius of the borehole showing the real radius of the borehole and the radius of the fitted ellipse.

Figure 4.2 shows the derived S_{max} and S_{min} orientation along the boreholes SB 2.2 and SB 2.3. A comparison of the two inclined SB boreholes indicates different stress conditions. In general, both boreholes show similar trends, with the mean S_{max} azimuth of 87° ± 30°N (SB 2.2) and at 61° ± 28°N (SB 2.3)(Table 4.2). In SB 2.2, the stress shows a homogeneous distribution as the stress seems to settle with the depth. In contrast, the stress in SB 2.3 fluctuates more significantly, especially after execution of the Mini-frac tests. Both boreholes show a higher distribution of the data in the area of the borehole top (ca. <20 m). However, there is a trend visible in the scattered data suggesting that S_{max} in the top 5 m of the borehole is rotating parallel to the tunnel axis (317°). In general, the boreholes indicate that the stress orientation becomes more uniform with depth. However, near fractures a significant stress re-orientation is observed.

Table 4.2 summarizes the results of the S_{max} azimuth in the different boreholes. The values for the Table are calculated using the circular mean and standard deviation, as the arithmetic mean and standard deviation do not respect the cyclic circular orientation.

Table 4.2: Overview of the S_{max} azimuth in the different boreholes derived by the Ellipticity analysis. The data points inside the casing were neglected.

	Before Mini-frac S_{max} azimuth [°]	Between Mini-frac S_{max} azimuth [°]	After Mini-frac S_{max} azimuth [°]	Total S_{max} azimuth [°]
SB 2.2	107 ± 26	82 ± 19	73 ± 25	87 ± 30
SB 2.3	67 ± 25	-	53 ± 31	61 ± 28
BFE_A_05	-	-	-	151 ± 23

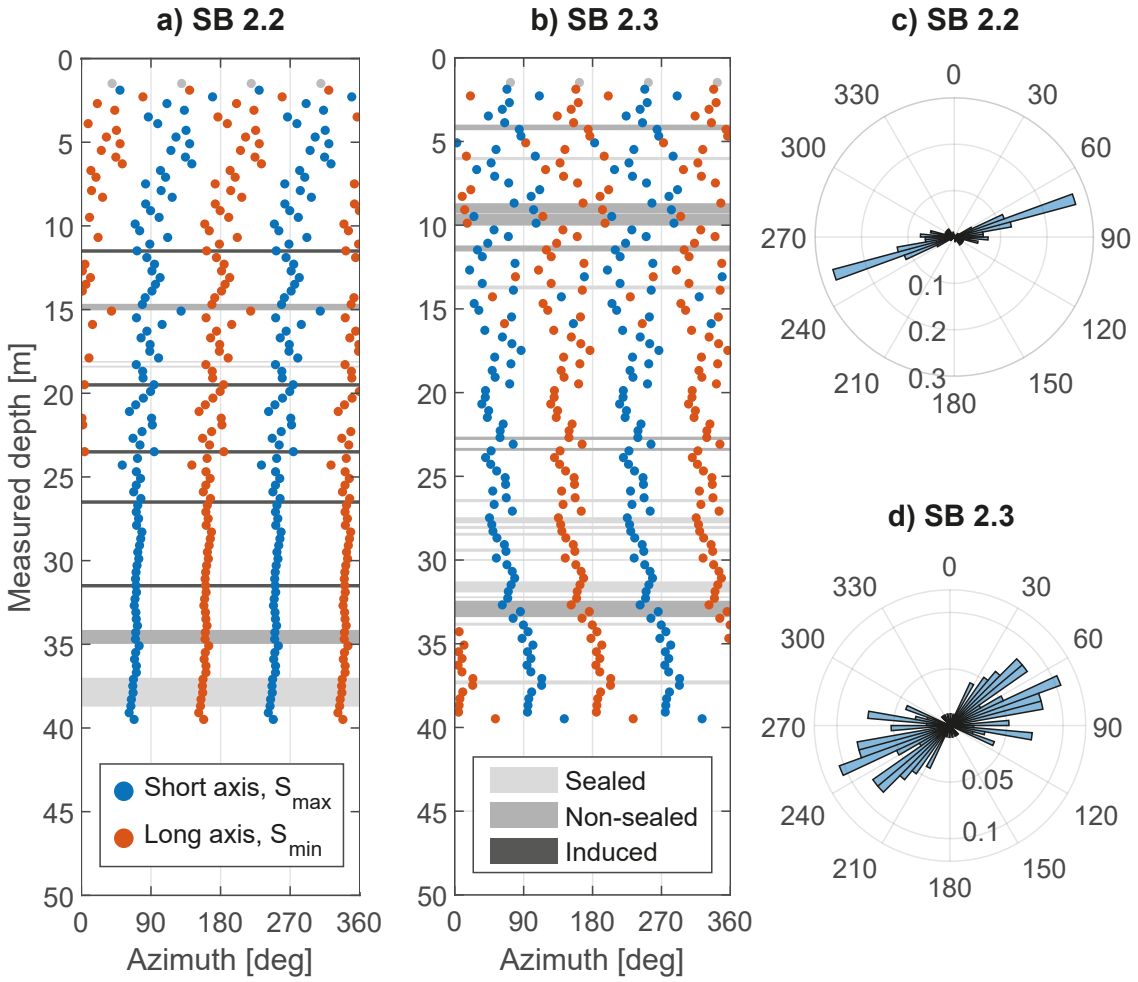

Figure 4.2: Ellipticity analysis of SB 2.2 and SB 2.3. Figure **a)** shows the orientation of the axes along the SB 2.2 borehole on 21.04.2019 in between the Mini-frac experiments (with five out of six fractured intervals). In contrast, figure **b)** shows the orientation of the axes along the SB 2.3 borehole on 08.03.2019 before the Mini-frac experiments. Data points within the casing are colored transparent with grey. The rose plots **c)** and **d)** display the short axes of the fitted ellipse.

The different logging data sets from borehole SB 2.2 are shown in Figure 4.3. Results for borehole SB 2.3 are attached in the Appendix A.3. The stress orientation in the boreholes varies over the observed time. Generally, the trend of S_{max} towards the east direction does not significantly

changed. Mini-frac tests were carried out between the ATV-logging (Chapter 2) and have induced new fractures. The induced fractures apparently lead to a significant stress orientation in the proximity. The chronological relations of the Mini-frac tests to the borehole ATV logs are shown in Figure 2.1. It can be summarised, that the stress azimuth rotates in the area of natural and induced fractures (Figure 4.3 and Appendix Figure A.3).

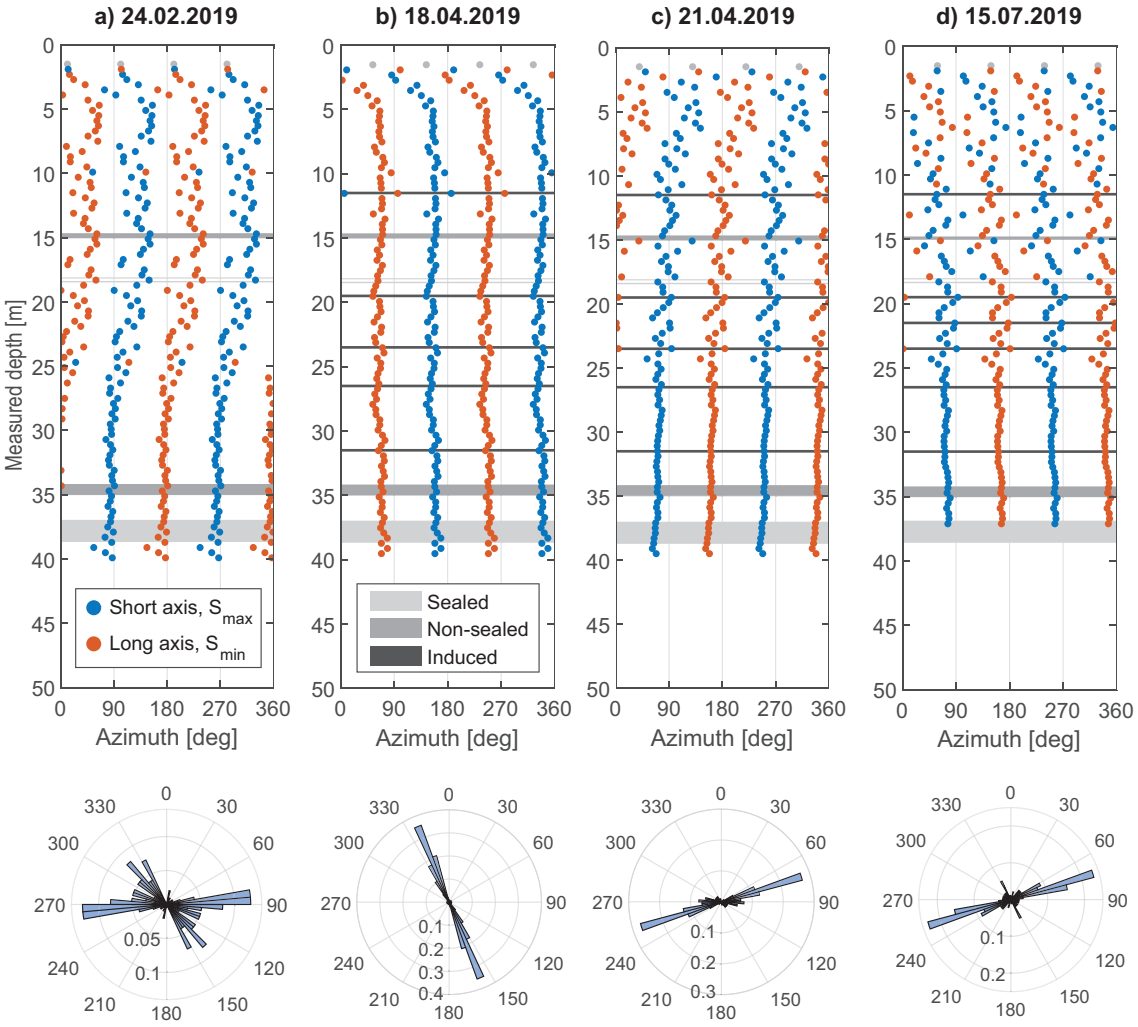

Figure 4.3: Ellipticity analysis of SB 2.2. The rose plots display the short axes of the fitted ellipse. Figure **a)** shows the orientation of the fitted ellipse axes before the Mini-frac tests, while **b)** and **c)** show the data in between the two Mini-frac experiments, when five from six intervals were already fractured. Therein, **b)** shows the erroneous data set with the mechanical problems of the centralizer, **d)** displays the fitted ellipse axes after the Mini-frac tests. Data points within the casing are colored transparent with grey.

Figure 4.4 shows the Ellipticity analysis performed on borehole BFE_A_05. It strengthens the major role of fractures on in-situ stress orientation. In particular, regions in and near fault zones show a substantial change in stress orientation and a rotation up to 30°. It appears, that fault zones serve as a transition between different stress regimes. For instance, in borehole BFE_A_05 zone 1, the azimuth of S_{max} shows significant variances of 147° ± 27°N, which is separated by the fault zone I. The azimuth of S_{max} in zone 2 shows a homogeneous trend of 150° ± 19°N. In contrast, the next zone 3, shows a higher azimuth variation with 147° ± 30°N and a general counterclockwise rotation of the S_{max} azimuth with depth. Finally, zone 4 exhibits homogeneous trend of S_{max} at 165° ± 12°N but a significantly higher average S_{max} azimuth than in the rest of the borehole. The stress azimuth within the zone shows first a counterclockwise and then a clockwise rotation.

The axis ratio tends to increase with depth, meaning that the magnitude of S_{min} and S_{max} align gradually. In addition, the axis ratio reveals different behaviour of the different zones. Zone 1 followed by zone 2 shows the lowest axis ratio and generally a broad distribution of data points. On the other hand, zone 3 and 4 show a relatively homogeneous high ratio. The axis ratio within the different fault zones shows a broad distribution of the values, indicating difficulties with the ellipse fitting as the borehole wall is disturbed.

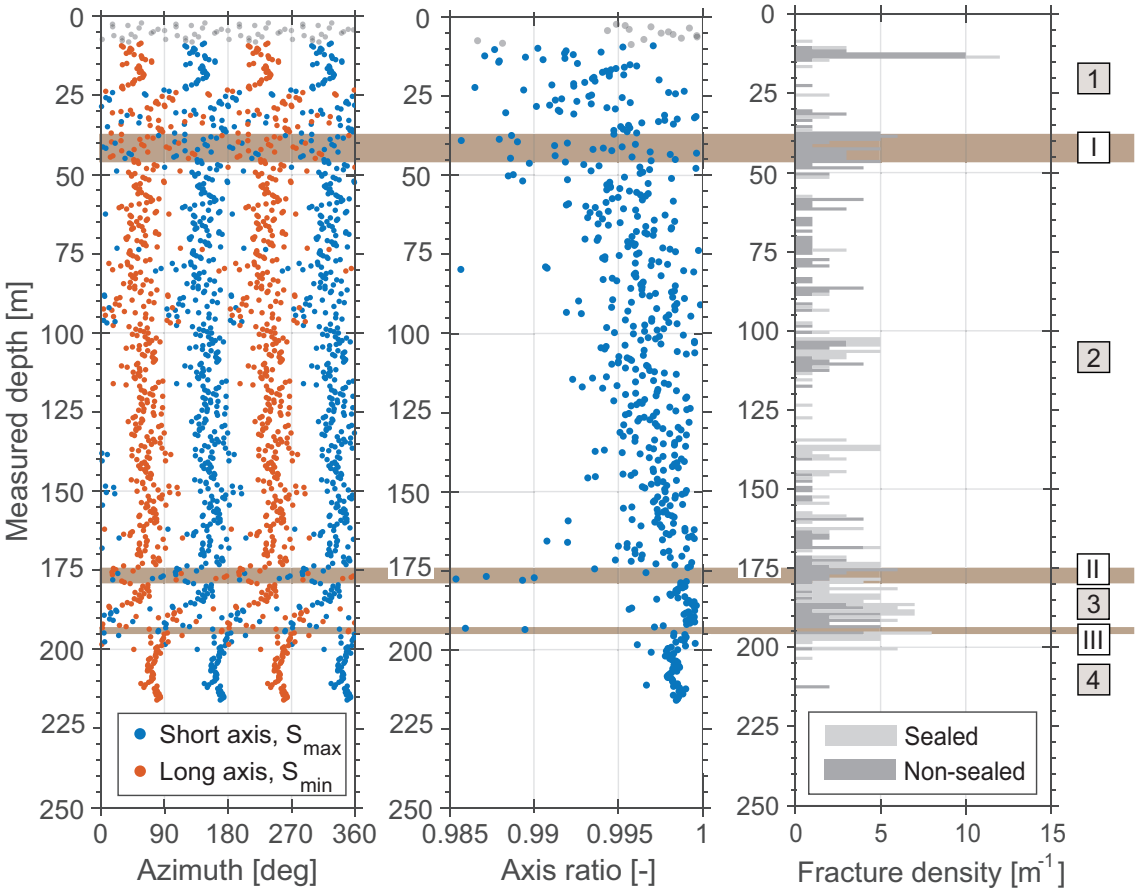

Figure 4.4: Correlation between Ellipticity analysis and the fracture density of borehole BFE_A_05. With brown, the major faults are highlighted and numbered in latin, while with greek numbers, the different stress regimes are shown. Data points within the casing are colored transparent with grey. The histogram includes the classification of the following fracture: Open fractures, undifferentiated, biotite filled and dykes. Fault zones were classified as areas with increased to high fracture density, in the log, a clear fractures trace with a high aperture is visible.

The distribution of the S_{max} azimuth of the borehole BFE_A_05 is shown in the Appendix A.4. S_{max} data points tend to be oriented in the direction of 151° ± 23°N. However, S_{max} data lying within the faults zone do not reveal the same trend and appear to occur unsystematically along the borehole wall (Appendix Figure A.4).

An illustrated overview of the detailed Ellipticity analysis for the different data sets of BFE_A_5, SB 2.2 and SB 2.3 is attached in the Appendix (Figure A.5-A.12). The Figures include the stress difference calculated from equation 4.3 and standard deviation. The stress difference shows a similar trend to the axis ratio. Variations along the borehole profile indicate, that the in-situ stress magnitude varies in the proximity of natural and induced fractures. Furthermore, it is notable that non-sealed fractures and induced fractures have a greater impact on stress magnitude than filled (sealed) fractures.

Appendix A.6 shows the Ellipticity analysis of BFE_A_05 in respect to the borehole high side (HS), compared to Appendix A.5 with respect to the NM. It can be seen that the log orientation has no major influence on the analysis and is simply a constant shift depending on the borehole azimuth.

4.3 Discussion

The results show that Ellipticity analysis allows an high-resolution estimation of the stress orientation of the investigated boreholes. The advantage of this method is that it allows stress analysis along the entire borehole, providing that the borehole wall is intact and not disturbed by fractures, breakouts, fault zones, washouts or drilling-induced perturbations.

The results show a S_{max} orientation of 77° ± 29°N in the investigated SB 2.2 and SB 2.3 boreholes located within the BULGG niche, in the FEAR area (TM 2363) the S_{max} value is 151° ± 23°N. However, the boreholes are inclined, making a comparison of the stress orientation to the far field stress and horizontal stress components challenging.

Nevertheless, the significant differences between the SB and FEAR areas are remarkable. One possible reason for the significant difference could arise from spatial variations in the stress field, i.e., the overburden in the FEAR area is about 100m higher than in the SB boreholes, which can influence prevailing stress conditions. Furthermore, different boreholes inclination and its azimuth relative to the stress field, can effect the borehole stability (Zoback, 2007; Ong and Roegiers, 1993). In BFE_A_05 the azimuth is oriented NE, while the SB boreholes are oriented towards SW.

Comparison with previous in-situ stress studies of the BedrettoLab

In her master thesis (Epiney, 2022) performed seismic cross-hole measurements between SB 2.1, 2.2 and 2.3 and observed a seismic anisotropy indicating a S_{hmin} of 153°N. Bröker and Ma (2022) investigated the trace of Mini-frac tests induced fractures in the SB 1.1, 2.1, 3.1 and 4.1 boreholes (TM 1750 - 2140). This led to an inference of the orientation of S_{Hmax} (100 - 120°N). van Limborgh (2020) carried out an ellipticity and borehole breakout analysis within his master thesis in the nearby CB1 and CB2 boreholes (TM 2043 and 2050), resulting in an observation of stress rotation around fracture zones and orientation of S_{hmin} of 190 - 195°N. Hence, the results found within this thesis are consistent with the previously found results of the stress orientation in the BedrettoLab. Therefore, the results obtained in this thesis are in the same range as previously found results. However, the results should be compared with a grain of salt, as these results within this study are from inclined boreholes and therefore do not correspond to the maximum principal stress.

In-situ stress variation

However, it is evident from the results that there appears to be a trend of the stress condition inside the tunnel. Notably, the fractures and fault zone occurrences influence and change significantly the stress orientation. Near fractures and fault zones, a rotation of the stress orientation and change of axis ratio is observed, correlating with with field observations (van Limborgh, 2020). Zhang and Ma (2021) have quantitatively modelled the stress rotation across fault zone rock mass. They have observed a stress rotation towards an 45° angle relative to the the fault plane. This trend could be confirmed in the boreholes of this study. Impacts from fractures and fault zones on the stress difference could be confirmed likewise. However, no evaluation could be made within the strongly deformed fault zone, as the fitting of the ellipse in this area is limited by the heavy rock deformation. Remarkably, the fractures induced by the Mini-frac experiments lead to a significant rotation of the S_{max} azimuth and change of axis ratio. The results in general, show a higher dispersion towards the top of the borehole (0 - 20 m), which could be caused by the stress redistribution from

the lack of rock material of the tunnel, temperature and drainage effects of the tunnel (Rutqvist, 2016; Arjnoi et al., 2009; Evans et al., 2003). On the top 5 m of the borehole a rotation of S_{max} towards the tunnel axis (317°) is observed. This agrees with a theoretical predicted stress rotation of S_{Hmax} towards the tunnel parallel axis (Fu et al., 2018). An excavation-induced influence of the drill and blast technique used during tunnel construction can mainly be expected at the borehole top 0 - 0.5 m (Martino and Chandler, 2004).

BFE_A_05 shows that abrupt changes in stress conditions occur around fault zones that can be recognised in the orientation as well as in the ratio of the stress. On the other hand, the stress between the fault zones shows similar behaviour and therefore can be classified into different stress regimes differentiated by fault zones.

Furthermore, SB 2.2 and 2.3 show that Mini-frac experiments impact the local stress field. Thus, a different stress profile is observed along the boreholes after performing the Mini-frac tests. In particular, in the intervals where the Mini-frac tests were performed, the borehole geometry changed, resulting in an in-situ stress reorientation. Specifically, stress rotation is noticeable in the area of the newly induced fractures.

In addition, the Ellipticity method was further extended based on an ellipse fitting to the ATV amplitude (Appendix Figures A.13 - A.15). The intention is to identify the stress concentration in the direction of S_{max}, as the rearrangement changes the elastic properties of the rock. This could be recognisable as a change of the amplitude from the reflected acoustic waves. The results suggest a more uniform elliptical behaviour of the data. However, there are significant ellipse rotations in the different data sets visible. This suggests that other factors such as tool centralisation and damage-induced rock deformation could have a more major impact.

Limitations of the method

Furthermore, the data show a high standard deviation caused by local stress anomalies on the one hand, and on the other hand, they reveal limitations of the method. The method is based on fitting an ellipse through the borehole geometry, a simplification that is not precise for all borehole geometries. Hence, minor changes in borehole shape can lead to major discrepancies in the ellipse orientation, resulting in inherent data scattering. Implying that the method is strongly dependent on the good quality of the ATV data.

The RMS error was calculated to evaluate the quality of the ellipse fitting. A lower value thereby indicates a better fitting. The results (Figure 4.5) show that fractures and fault zones affect the quality of the ellipse fitting, especially in fault zones where the borehole shape is disturbed. Implicitly, the ellipse fitting algorithm systematically struggles in these intervals. This is also reflected by the unsystematic stress orientation within the fault zones (Appendix figure A.4). Moreover, drilling-induced perturbations on the borehole wall can impair the quality of the ellipse fitting. The quality of the ATV data varies between the data sets. However, there is a consistent RMS shift along the borehole across all data sets of each borehole. This could indicate that the mechanical centralizer did not always optimally centralise the tool.

The borehole deformation is based on the simplified ideal assumption that the deformation of the rock behaves linearly elastic until its failure. The calculation of stress difference was made under the assumption that Young's modulus, Poisson's ratio and initial borehole diameter are constant. This is a simplification, as these parameters can change spatial within the borehole due to natural heterogeneities and drilling-induced effects. Since the deformation of the rock is time-dependent, Young's modulus, Poisson's ratio and initial borehole diameter can vary over time, this time-dependent effect on these parameters was not taken into account, assuming that the borehole was completely deformed (Han et al., 2021).

These limitations are also reflected in the calculated stress difference profile along the borehole. The calculated stress difference values are much higher then what is expected from the Mini-frac analysis. This shows that the borehole deforms more than assumed and the linear elastic borehole deformation and constant initial borehole diameter correspond to a strong simplifications in the technique, leading to a high stress difference. Hence, calculating the stress difference based on calculated deformations of the ATV data is a unsuitable and a relative stress magnitude description based on the axis ratio is a more appropriate method for this application.

Other potential causes of changes in the stress field along the borehole may be due to mineralogical anomalies in the rock, but this was not further analysed during this thesis (Hofmann et al., 2015; Ismail and Zoback, 2016).

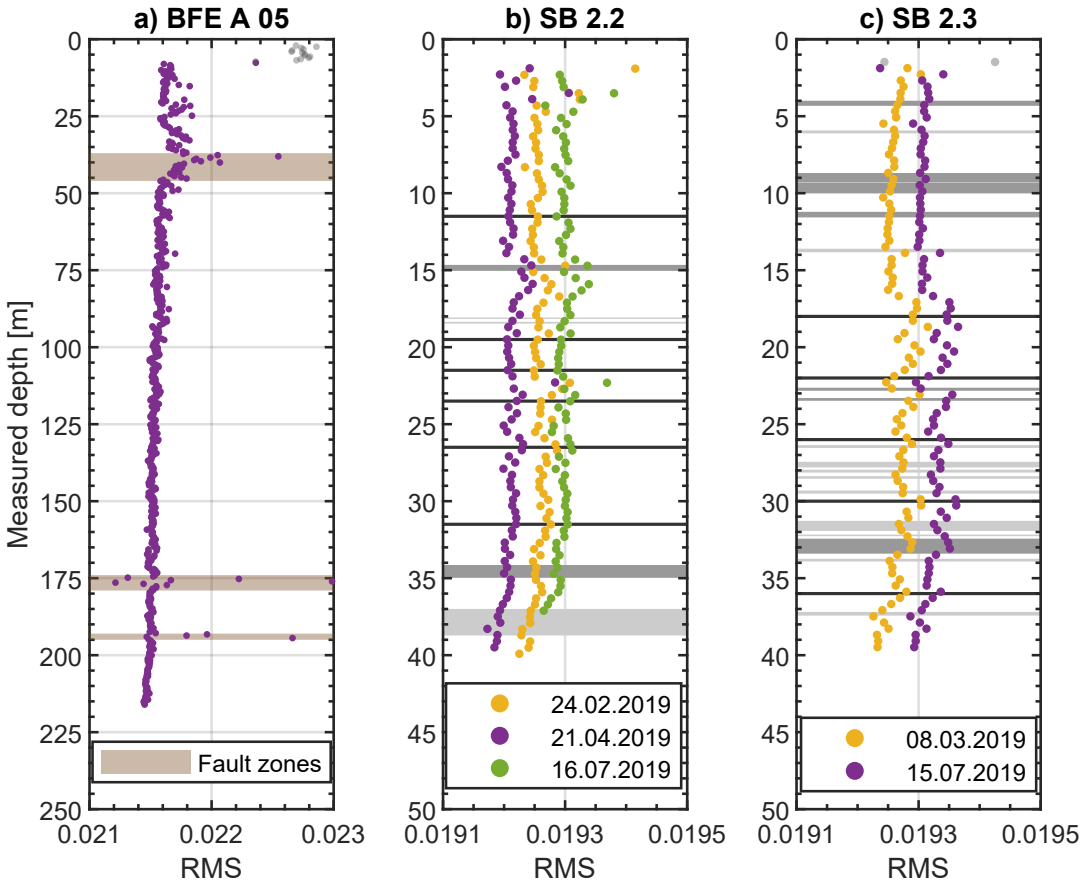

Figure 4.5: Calculated RMS to evaluate the quality of the elliptical fitting of the boreholes BFE_A_05 (**a**), SB 2.2 (**b**) and SB 2.3 (**c**). Data points within the casing are colored transparent with grey.

In-situ stress complementing using Ellipticity and Mini-frac analysis

Merging the in-situ stress measurements from the Ellipticity analysis with the Mini-frac results (Figure 4.6) allows for a more comprehensive stress description in the boreholes, as these methods jointly indicate both the stress orientation and S_3 magnitude. In this relation, certain correlations can be observed. In the investigated SB 2.2 and SB 2.3 boreholes, the stress state changes at a measured depth of 20 - 25 m. The Ellipticity analysis reveals a stress change in this section. The stress orientation behaves more scattered at the borehole top (0 - 25 m), while further away (25 m to bottom), the orientation behaves more uniformly. The stress magnitude obtained by the Mini-frac tests confirms a stress change in the range of 20 - 25 m, likewise. A stress drop is

observed in this depth interval, while above S_3 increases and below this specific depth, the stress magnitude increases continuously towards the bottom. It remains unclear whether this described stress change is caused by the tunnel and the induced effects (drainage, temperature decrease) or due to the fracture presence.

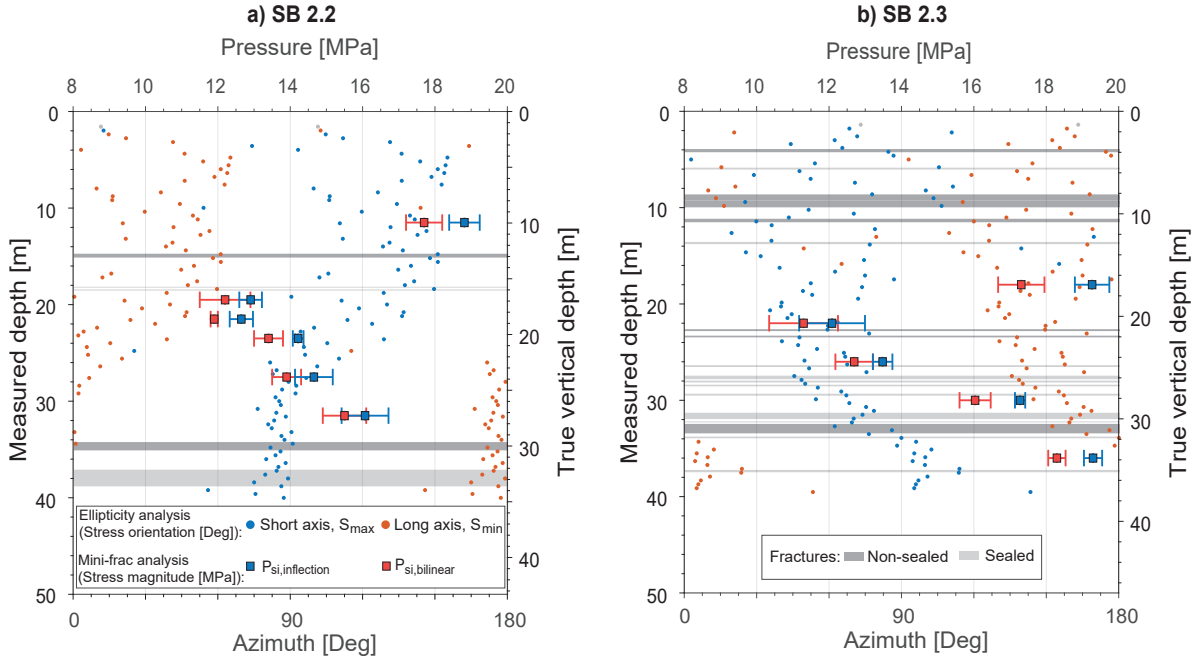

Figure 4.6: Combination of Ellipticity analysis and Mini-frac results. The Ellipticity data sets before the Mini-frac tests are shown (SB 2.2 24.02.2019 and SB 2.3 08.03.2019). The Ellipticity data shows the stress azimuth, illustrated with dots. The S_3 estimations are shown from the Mini-frac data, marked as squares. Data points within the casing are colored transparent with. **a)** reveals the in-situ stress state of SB 2.2. **b)** displays the stress condition in SB 2.3.

Conclusively, it can be stated that in the investigated SB 2.2, SB 2.3 and BFE_A_05 boreholes, stress variation occurs along the borehole. In particular, significant stress changes are observed in a measured depth interval of about 20 - 25 m.

Chapter 5

Conclusion and Outlook

The main conclusions of this thesis can be summarised as follows:

- Pressure transient analysis of the Mini-frac tests allow an estimation of the least principal stress magnitude. Resulting in the following S_3 magnitudes for the investigated inclined boreholes SB 2.2 and SB 2.3: $S_3 = 15.6 \pm 2.8$ MPa (using $P_{si,inflection}$) with $P_p = 2.5$ to 3.7 MPa, agreeing with magnitudes determined by Bröker and Ma (2022).
- Four different methods to describe the least principal stress magnitude have been applied and examined: Closure pressure, jacking pressure, bilinear pressure-decay and inflection point method on the shut-in pressure. They lead to comparable values. However, due to its steady applicability and reliability, the shut-in pressure was found to give the most accurate estimate.
- The borehole deformation can be described by using an ellipse shape. This simplification allows a stress orientation reconstruction. In this work, an innovative, promising approach was successfully applied using the ATV traveltime data to continuously map the total borehole length. Allowing stress changes to be identified easily with excellent vertical resolution.
- Based on the borehole deformation, the in-situ stress orientation could be estimated to be: $S_{max} = 77° \pm 29°$N (NM) (in SB 2.2 and SB 2.3) and $S_{max} = 151° \pm 23°$N (NM) (in BFE_A_05).
- Significant spatial in-situ stress variations have been observed and documented along and among the different boreholes. Furthermore, various stress regimes have been identified along the borehole, enabling a classification in the borehole into different zones with steady stress regimes, separated by stress change around fault zones.
- Multiple fractures and fault zones intersect the boreholes, strongly influencing the in-situ stress condition. Stress rotation and stress magnitude reduction has been found in the proximity of the fractures and fault zones. In particular, the new fractures induced by the Mini-frac tests revealed a stress rotation of up to 30°.
- Within the fracture and fault zones, the borehole is intensely deformed. For those areas, stress reconstruction with ellipse fitting is challenging.
- On top of the borehole (0 - 25 m, measured depth) a significant stress change was observed, within this depth a scattering of the stress direction was measured. While the Mini-frac tests revealed a significant S_3 magnitude drop in 20 - 25 m depth. In addition, on the top 5 m, a stress rotation of S_{max} in the direction of the parallel tunnel axis was observed.
- Summarised, two different in-situ stress measurement methods were applied within this thesis. The combination allowed a detailed profound description of the stress distribution and anomalies in the fractured crystalline rock mass. Concretely, a detailed in-situ stress profile along the borehole was developed, which indicates the stress magnitude and orientation.

Outlook

In the future, further investigations are planned in the Bedretto tunnel, providing an enhanced insight into the prevailing in-situ stress. The analysis could be extended and applied to other existing and additional planned boreholes along the Bedretto tunnel. Specifically, expanding the integration of the Ellipticity analysis on vertical boreholes could help to understand better the stress inversion. Furthermore, the methods could be extended to understand the impact of time-dependent rock deformation, influence of logging data quality and natural variability of the fractured rock mass. For this aim, a repeated logging campaign of the boreholes would be beneficial. Another possibility is extending the analysis with DCDA (Diametrical Core Deformation Analysis) to compare and verify the in-situ stress inference using the cores.

Moreover, it will be auspicious to compare the boreholes with other stress experiments to verify the obtained results. Mini-frac experiments are planned in the FEAR area, as well as hydraulic fracturing of pre-existing fractures (HFPF) through a new innovative Method (Step-rate Injection Method for Fracture In-situ Properties (SIMFIP)). Integration of the different methods could improve high resolution mapping of the in-situ stress. Our results highlight the relevance of more geomechnical research on the in-situ stress linked to tunnel-induced effects and fracture influence.

In brief, promising in-situ stress findings were obtained in this thesis. The BedrettoLab will be in operation for several more years, allowing further meaningful experiments in crystalline rock to improve the understanding of essential hydro-seismo-mechanical processes in the fractured crystalline underground.

Bibliography

Anderson, E. M. (1905). The dynamics of faulting. *Transactions of the Edinburgh Geological Society*, 8(3):387–402.

Arjnoi, P., Jeong, J. H., Kim, C. Y., and Park, K. H. (2009). Effect of drainage conditions on pore-water pressure distributions and lining stresses in drained tunnels. *Tunnelling and Underground Space Technology*, 24(4):376–389.

Baumgärtner, J. and Zoback, M. D. (1989). Interpretation of hydraulic fracturing pressure-time records using interactive analysis methods. *International Journal of Rock Mechanics and Mining Sciences & Geomechanics Abstracts*, 26(6):461–469.

Bell, J. S. and Gough, D. I. (1979). Northeast-southwest compressive stress in Alberta evidence from oil wells. *Earth and Planetary Science Letters*, 45(2):475–482.

Bredehoeft, J. D., Wolff, R. G., Keys, W. S., and Shuter, E. (1976). Hydraulic fracturing to determine the regional in situ stress field, Piceance Basin, Colorado. *Geological Society of America Bulletin*, 87(2):250–258.

Bröker, K. (2019). In-situ stress and rock mass characterization via mini-frac tests at the Bedretto Underground Laboratory.

Bröker, K. and Ma, X. (2022). Estimating the Least Principal Stress in a Granitic Rock Mass: Systematic Mini-Frac Tests and Elaborated Pressure Transient Analysis. *Rock Mechanics and Rock Engineering*.

Chang, C. and Jo, Y. (2015). Heterogeneous in situ stress magnitudes due to the presence of weak natural discontinuities in granitic rocks. *Tectonophysics*, 664:83–97.

Chong, J. (2021). Inferring in situ stress variations from post-drilling borehole diametrical deformation.

Cornet, F. H. and Valette, B. (1984). In situ stress determination from hydraulic injection test data. *Journal of Geophysical Research: Solid Earth*, 89(B13):11527–11537.

David, C. ., Nejati, M. ., and Geremia, D. (2020). On petrophysical and geomechanical properties of Bedretto Granite.

Doe, T. W. and Korbin, G. E. (1987). A comparison of hydraulic fracturing and hydraulic jacking stress measurements. *28th U.S. Symposium on Rock Mechanics (USRMS)*, pages 283–290.

Dutler, N., Valley, B., Gischig, V., Jalali, M., Brixel, B., Krietsch, H., Roques, C., and Amann, F. (2020). Hydromechanical insight of fracture opening and closure during in-situ hydraulic fracturing in crystalline rock. *International Journal of Rock Mechanics and Mining Sciences*, 135:104450.

Epiney, C. (2022). Investigating anisotropic seismic velocities of the Rotondo granite in intact and fractured sections by crosshole seismic surveys.

Evans, K., Dahlø, T., and Roti, J. A. (2003). Mechanisms of pore pressure-stress coupling which can adversely affect stress measurements conducted in deep tunnels. *Pure and Applied Geophysics*, 160(5-6):1087–1102.

Fu, P., Kneafsey, T. J., Morris, J. P., and White, M. D. (2018). Predicting hydraulic fracture trajectory under the influence of a mine drift in EGS Collab Experiment I. Technical report.

Funato, A., Ito, T., and Shono, T. (2012). Laboratory Verification of the Diametrical Core Deformation Analysis (DCDA) Developed For In-situ Stress Measurements.

Gischig, V. S., Giardini, D., Amann, F., Hertrich, M., Krietsch, H., Loew, S., Maurer, H., Villiger, L., Wiemer, S., Bethmann, F., Brixel, B., Doetsch, J., Doonechaly, N. G., Driesner, T., Dutler, N., Evans, K. F., Jalali, M., Jordan, D., Kittilä, A., Ma, X., Meier, P., Nejati, M., Obermann, A., Plenkers, K., Saar, M. O., Shakas, A., and Valley, B. (2020). Hydraulic stimulation and fluid circulation experiments in underground laboratories: Stepping up the scale towards engineered geothermal systems. *Geomechanics for Energy and the Environment*, 24:100175.

Gronseth, J. M. and Kry, P. R. (1981). Instantaneous shut-in pressure and its relationship to the minimum in situ stress. In *Proc. USGS Workshop on Hydraulic Fracture Stress Measurement*, pages 147–166. Citeseer.

Haimson, B. C. and Cornet, F. H. (2003). ISRM suggested methods for rock stress estimation-part 3: Hydraulic fracturing (HF) and/or hydraulic testing of pre-existing fractures (HTPF).

Halır, R. and Flusser, J. (1998). Numerically stable direct least squares fitting of ellipses. In *Proc. 6th International Conference in Central Europe on Computer Graphics and Visualization. WSCG*, volume 98, pages 125–132. Citeseer.

Han, H., Yin, S., Chen, Z., and Dusseault, M. B. (2021). Estimate of in-situ stress and geomechanical parameters for Duvernay Formation based on borehole deformation data. *Journal of Petroleum Science and Engineering*, 196.

Han, H. X. and Yin, S. (2018). Determination of in-situ stress and geomechanical properties from borehole deformation. *Energies*, 11(1).

Heidbach, O., Rajabi, M., Reiter, K., and Ziegler, M. (2016). World Stress Map 2016.

Hofmann, H., Babadagli, T., Yoon, J. S., Zang, A., and Zimmermann, G. (2015). A grain based modeling study of mineralogical factors affecting strength, elastic behavior and micro fracture development during compression tests in granites. *Engineering Fracture Mechanics*, 147:261–275.

Hubbert, M. K. and Willis, D. G. (1957). Mechanics of hydraulic fracturing. *Transactions of the AIME*, 210(01):153–168.

Ismail, M. I. and Zoback, M. D. (2016). Effects of rock mineralogy and pore structure on stress-dependent permeability of shale samples. *Philosophical Transactions of the Royal Society A: Mathematical, Physical and Engineering Sciences*, 374(2078).

Jordan, D. (2019). Geological Characterization of the Bedretto Underground Laboratory for Geoenergies.

Keller, F. and Schneider, T. R. (1982). Geologie und geotechnik. *Schweizer Ingenieur und Architekt*, 24:82.

Kirsch, C. (1898). Die theorie der elastizitat und die bedurfnisse der festigkeitslehre. *Zeitschrift des Vereines Deutscher Ingenieure*, 42:797–807.

Klee, G., Bunger, A., Meyer, G., Rummel, F., and Shen, B. (2011). In situ stresses in borehole Blanche-1/South Australia derived from breakouts, core discing and hydraulic fracturing to 2 km depth. *Rock Mechanics and Rock Engineering*, 44(5):531–540.

Lee, M. Y. and Haimson, B. C. (1989). Statistical evaluation of hydraulic fracturing stress measurement parameters. *International Journal of Rock Mechanics and Mining Sciences and*, 26(6).

Lützenkirchen, V. and Loew, S. (2011). Late Alpine brittle faulting in the Rotondo granite (Switzerland): Deformation mechanisms and fault evolution. *Swiss Journal of Geosciences*, 104(1).

Ma, X., Doonechaly, N. G., Hertrich, M., Gischig, V., and Klee, G. (2019). Preliminary in situ stress and fracture characterization in the Bedretto Underground Laboratory, Swiss Alps: implications on hydraulic stimulation. In *Rock Mechanics for Natural Resources and Infrastructure Development*, pages 1559–1567. CRC Press.

Ma, X., Hertrich, M., Amann, F., Bröker, K., Doonechaly, N. G., Gischig, V., Hochreutener, R., Kästli, P., Krietsch, H., Marti, M., Nägeli, B., Nejati, M., Obermann, A., Plenkers, K., Rinaldi, A. P., Shakas, A., Villiger, L., Wenning, Q., Zappone, A., Bethmann, F., Castilla, R., Seberto, F., Meier, P., Driesner, T., Loew, S., Maurer, H., Saar, M. O., Wiemer, S., and Giardini, D. (2022). Multi-disciplinary characterizations of the BedrettoLab-A new underground geoscience research facility. *Solid Earth*, 13(2):301–322.

Martino, J. B. and Chandler, N. A. (2004). Excavation-induced damage studies at the Underground Research Laboratory. *International Journal of Rock Mechanics and Mining Sciences*, 41(8):1413–1426.

McClure, M., Bammidi, V., Cipolla, C., Cramer, D., Martin, L., Savitski, A. A., Sobernheim, D., and Voller, K. (2019). A Collaborative Study on DFIT Interpretation: Integrating Modeling, Field Data, and Analytical Techniques. *SPE/AAPG/SEG Unconventional Resources Technology Conference 2020, URTeC 2020*.

McClure, M. W. (2022). Chapter 7 - Advances in interpretation of diagnostic fracture injection tests. In Moghanloo, R. G., editor, *Unconventional Shale Gas Development*, pages 185–215. Gulf Professional Publishing.

McClure, M. W., Biyton, C. A., Jung, H., and Sharma, M. M. (2014). The effect of changing fracture compliance on pressure transient behavior during diagnostic fracture injection tests. In *Proceedings - SPE Annual Technical Conference and Exhibition*, volume 7.

McClure, M. W., Hojung, J., Cramer, D. D., and Sharma, M. M. (2016). The fracture-compliance method for picking closure pressure from diagnostic fracture-injection tests. In *SPE Journal*, volume 21.

Meier, M. (2017). Geological characterisation of an underground research facility in the Bedretto tunnel.

Nolte, K. G. (1979). Determination Of Fracture Parameters From Fracturing Pressure Decline. *All Days*.

Ong, S. H. and Roegiers, J. C. (1993). Influence of anisotropies in borehole stability. *International Journal of Rock Mechanics and Mining Sciences and*, 30(7).

Rousopoulou, V. (2020). *Integrated geomechanics study of in situ stress and fracture system in the Bedretto Underground Lab: insights from a tripod of boreholes*. PhD thesis.

Rutqvist, J. (2016). Fractured rock stress-permeability relationships from in situ data and effects of temperature and chemical-mechanical couplings. *Crustal Permeability*, pages 65–82.

Rutqvist, J. and Stephansson, O. (1996). A cyclic hydraulic jacking test to determine the in situ stress normal to a fracture. *International Journal of Rock Mechanics and Mining Sciences & Geomechanics Abstracts*, 33(7):695–711.

Schmitt, D. R. and Haimson, B. (2017). Hydraulic fracturing stress measurements in deep holes. *Rock mechanics and engineering 1*, pages 183–225.

Stephansson, O. (1983). Rock Stress Measurement By Sleeve Fracturing.

van Limborgh, R. (2020). Borehole Indicators of In Situ Stress Field Heterogeneity at the Bedretto Underground Laboratory.

Zang, A. and Stephansson, O. (2010). Rock Fracture Criteria. *Stress Field of the Earth's Crust*, pages 37–62.

Zhang, S. and Ma, X. (2021). How Does In Situ Stress Rotate Within a Fault Zone? Insights From Explicit Modeling of the Frictional, Fractured Rock Mass. *Journal of Geophysical Research: Solid Earth*, 126(11):e2021JB022348.

Zhang, S., Niu, X., Yin, S., and Ru, Z. (2016). Estimation of earth stresses and fracture properties using numerical method and soft computing. Technical Report 4.

Zhang, S. and Yin, S. (2014). Determination of in situ stresses and elastic parameters from hydraulic fracturing tests by geomechanics modeling and soft computing. *Journal of Petroleum Science and Engineering*, 124:484–492.

Ziegler, M. and Valley, B. (2021). Evaluation of the Diametrical Core Deformation and Discing Analyses for In-Situ Stress Estimation and Application to the 4.9 km Deep Rock Core from the Basel Geothermal Borehole, Switzerland. *Rock Mechanics and Rock Engineering*, 54(12).

Zoback, M. D. (2007). *Reservoir Geomechanics*.

Zoback, M. D., Barton, C. A., Brudy, M., Castillo, D. A., Finkbeiner, T., Grollimund, B. R., Moos, D. B., Peska, P., Ward, C. D., and Wiprut, D. J. (2003). Determination of stress orientation and magnitude in deep wells. *International Journal of Rock Mechanics and Mining Sciences*, 40(7-8):1049–1076.

Appendix A

Supplementary Information

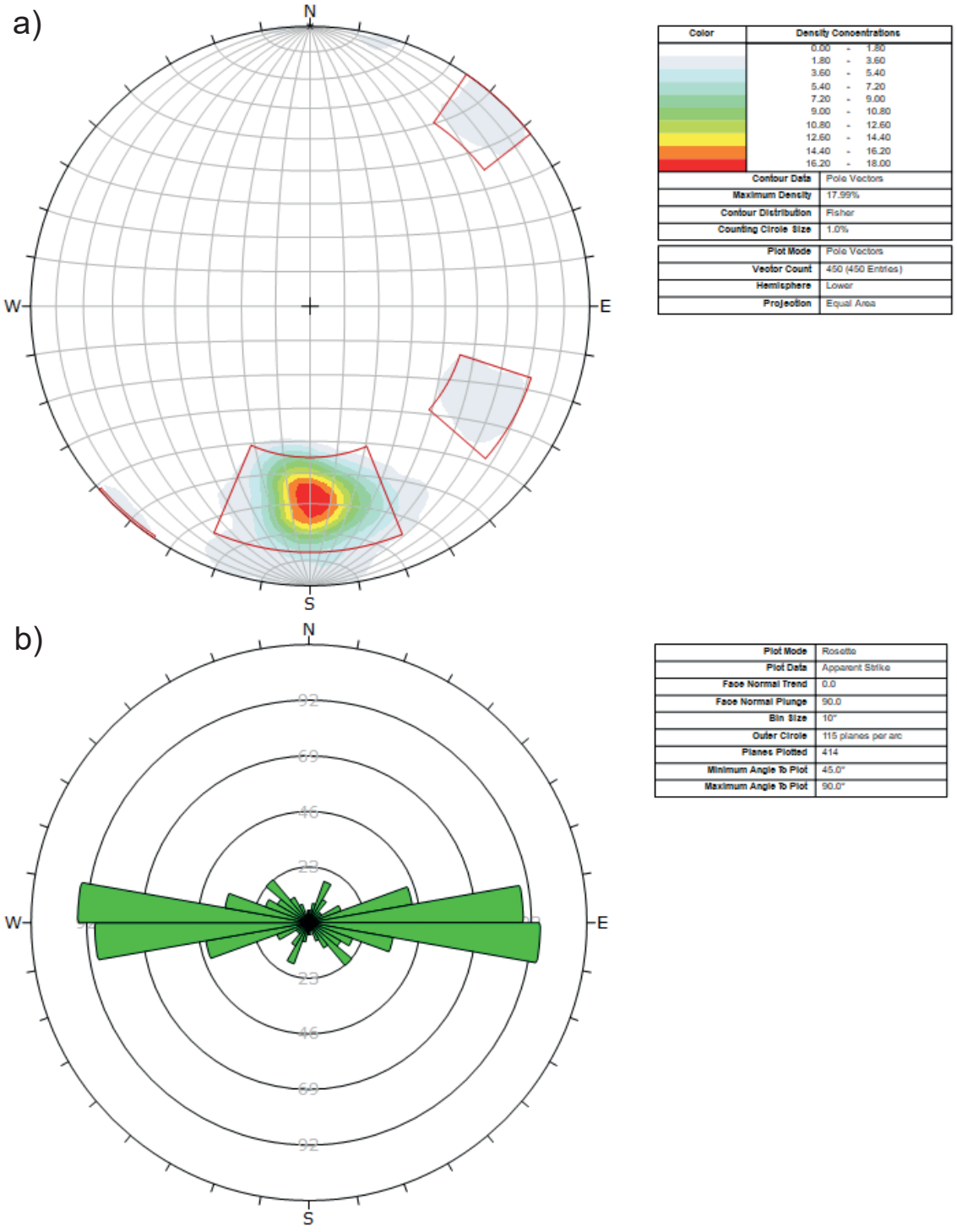

Figure A.1: Orientation of the geological structures of borehole BFE_A_05. **a)** Stereonet displaying the poles (in dip/dip direction) of the picked structures. **b)** Rose plot showing the strike of the structures.

Table A.1: Overview of the various determined pressure values in borehole SB 2.2 and 2.3.

Borehole	Measured depth [m]	$P_{cl,compliance}$ [MPa]	$P_{si,inflection}$ [MPa]	$P_{si,bilinear}$ [MPa]	$P_{jacking}$ [MPa]	P_b [MPa]	P_r [MPa]	P_p [Mpa]	T [Mpa]
SB 2.2	11.5	10.5	18.8 ± 0.4	17.7 ± 0.5	18.3	27.7	17.7	2.5	10.0
	19.5	12.5	12.9 ± 0.3	12.2 ± 0.7	13.5	18.5	12.9	-	5.6
	21.5	10.0	12.6 ± 0.3	11.9 ± 0.1	13.1	18.5	13.0	-	5.5
	23.5	11.5 ± 0.5	14.2 ± 0.1	13.4 ± 0.4	14.3	22.0	15.0	-	7.0
	27.5	11.8 ± 0.3	14.7 ± 0.5	13.9 ± 0.4	14.1	22.7	15.6	-	7.1
	31.5	14.2 ± 0.5	16.1 ± 0.6	15.5 ± 0.6	-	25.0	16.7	3.1	8.3
SB 2.3	18.0	-	19.3 ± 0.5	17.3 ± 0.6	-	33.3	22.6	2.7	10.7
	22.0	-	12.1 ± 0.9	11.3 ± 1.0	-	16.8	10.6	-	6.2
	26.0	11.9 ± 0.2	13.5 ± 0.3	12.7 ± 0.5	15.2	24.2	15.7	-	8.5
	30.0	14.6 ± 0.2	17.3 ± 0.1	16.0 ± 0.4	17.2	27.6	15.5	-	12.1
	36.0	17.3 ± 0.4	19.3 ± 0.3	18.3 ± 0.2	-	28.9	18.8	3.7	10.1

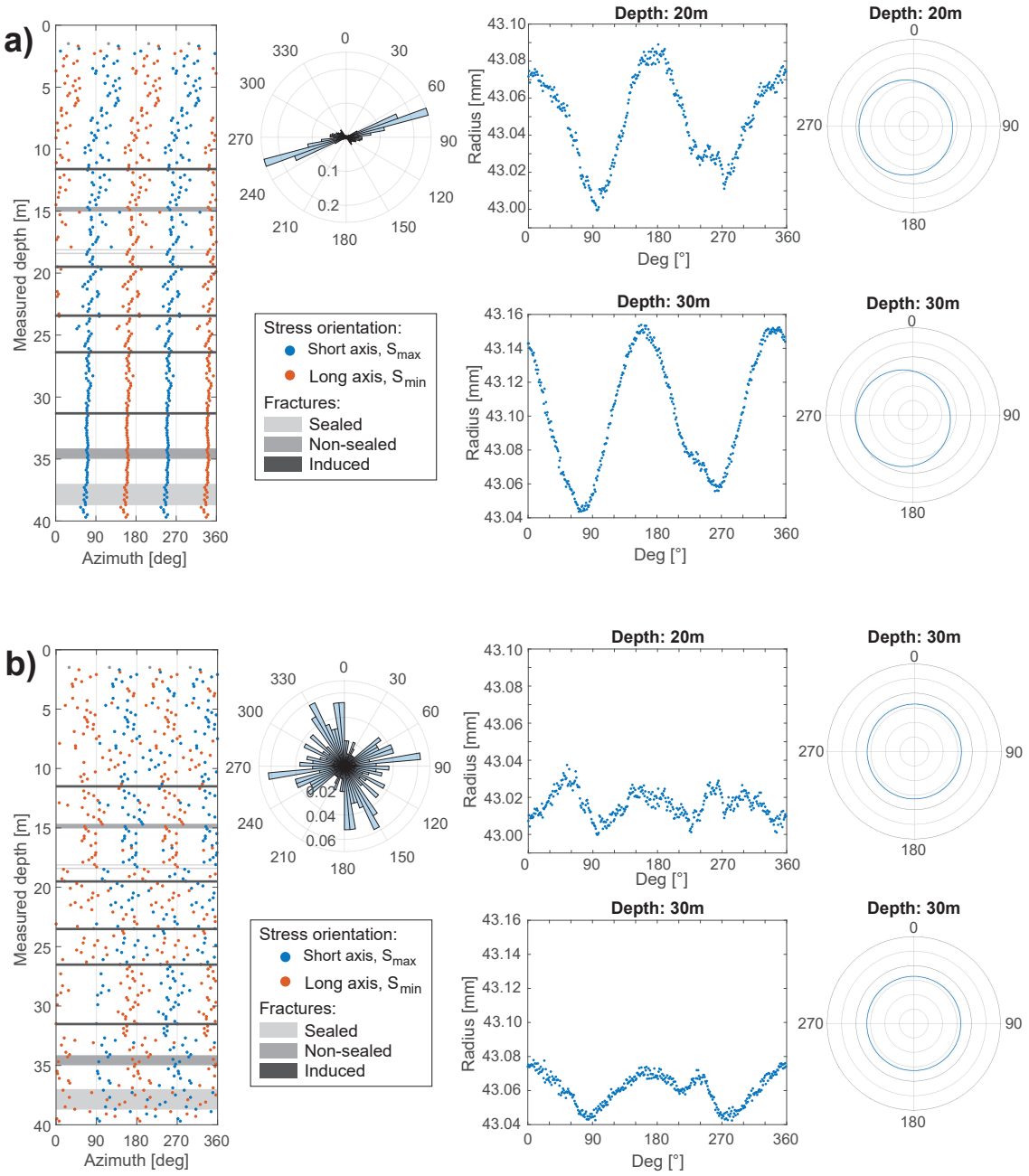

Figure A.2: Effect of centralisation on the Ellipticity analysis in SB 2.2 (data set 21.04.2019, when five from six Mini-frac intervals were fractured). The rose plots display the short axes of the fitted ellipse, the right shows the radius of the borehole and the cross-section on two depth examples 20 and 30 m. Data points within the casing are colored transparent with grey. **a)** shows the raw data set, while **b)** displays the centralized data. It can be seen that the centralisation causes the borehole to be centred and hence reduces the elliptical trend, resulting in the stress orientation determination becoming more diffuse.

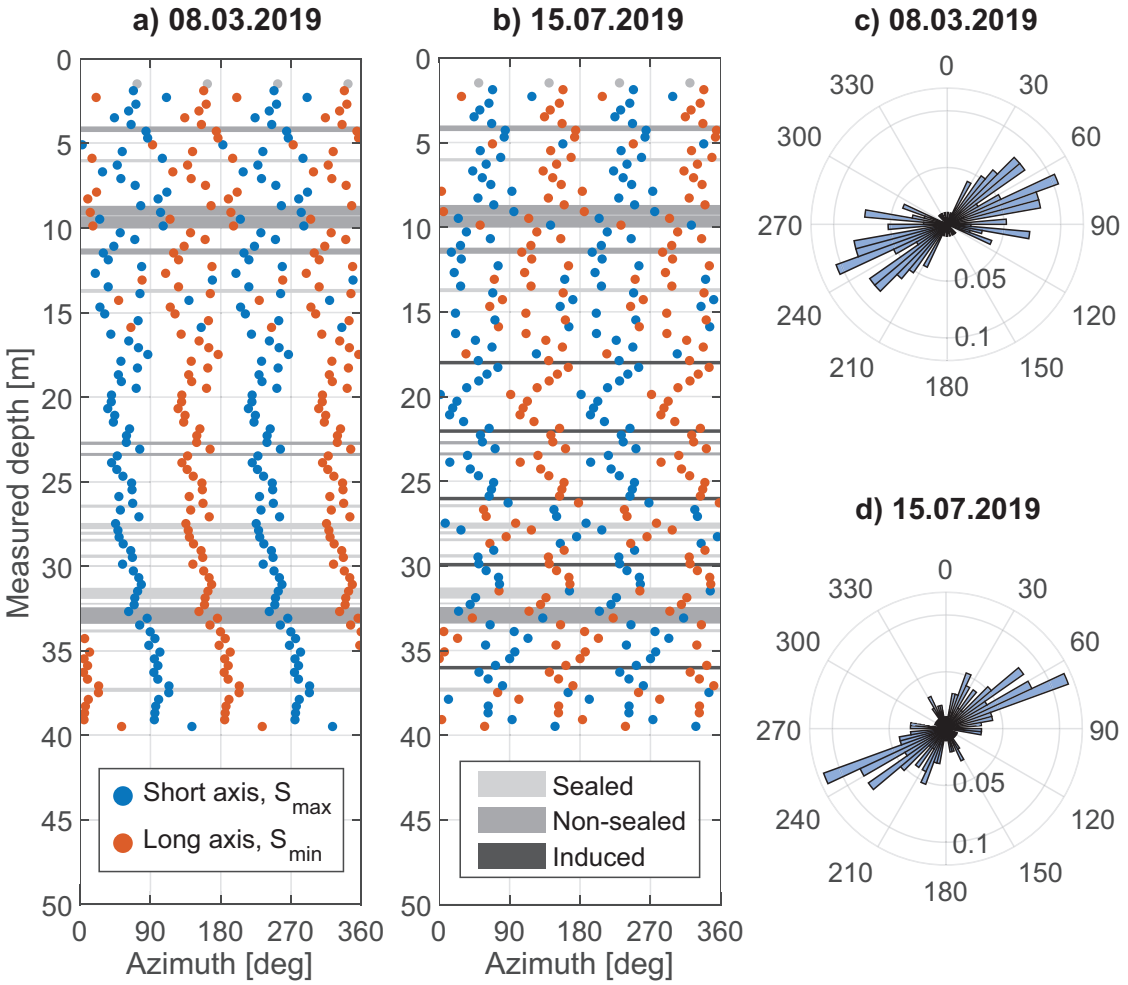

Figure A.3: Ellipticity analysis of SB 2.3. The rose plots display the short axes of the fitted ellipse. Whilst **a)** and **c)** shows the orientation of the fitted ellipse axes before the Mini-Frac tests logged by the ATV run at 08.03.2019, **b)** and **d)** show the orientation of the fitted ellipse axes after the Mini-Frac tests from the ATV logging of 15.07.2019. Data points within the casing are colored transparent with grey.

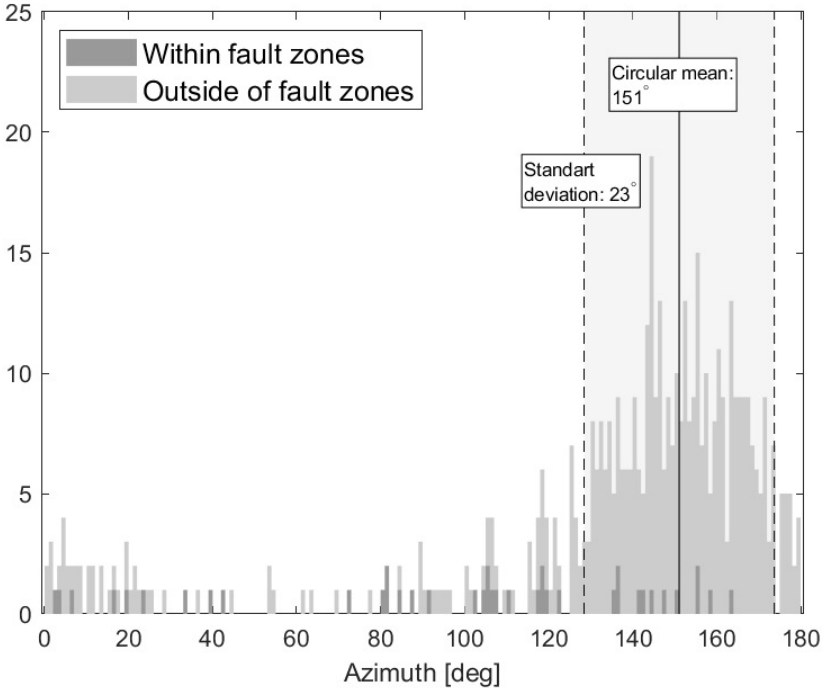

Figure A.4: S_{max} histogram of the borehole BFE_A_05. It is visible that the S_{max} azimuth laying within the fault zones is less sorted distributed compared to S_{max} azimuth laying outside of the fault zones.

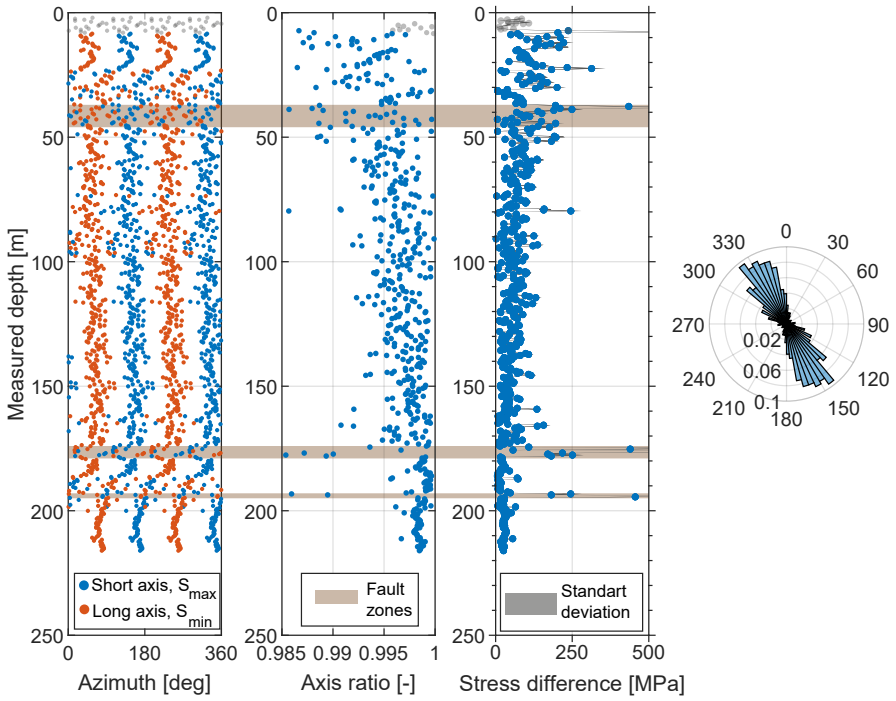

Figure A.5: Ellipticity analysis of BFE_A_05 in respect to Magnetic North. The rose plots display the short axes of the fitted ellipse. Data points within the casing are colored transparent with grey.

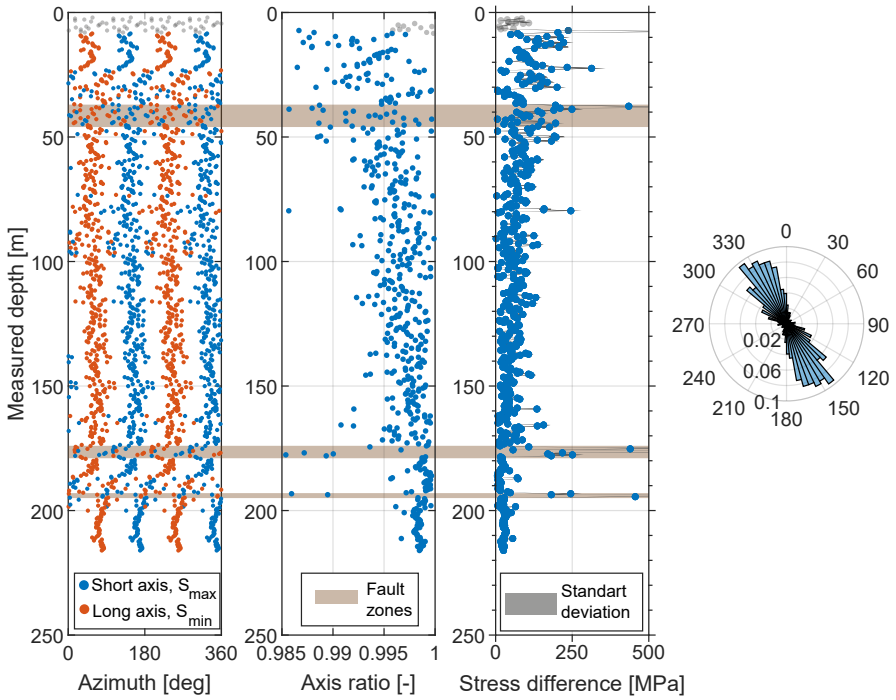

Figure A.6: Ellipticity analysis of BFE_A_05 in respect to high side. The rose plots display the short axes of the fitted ellipse. Data points within the casing are colored transparent with grey.

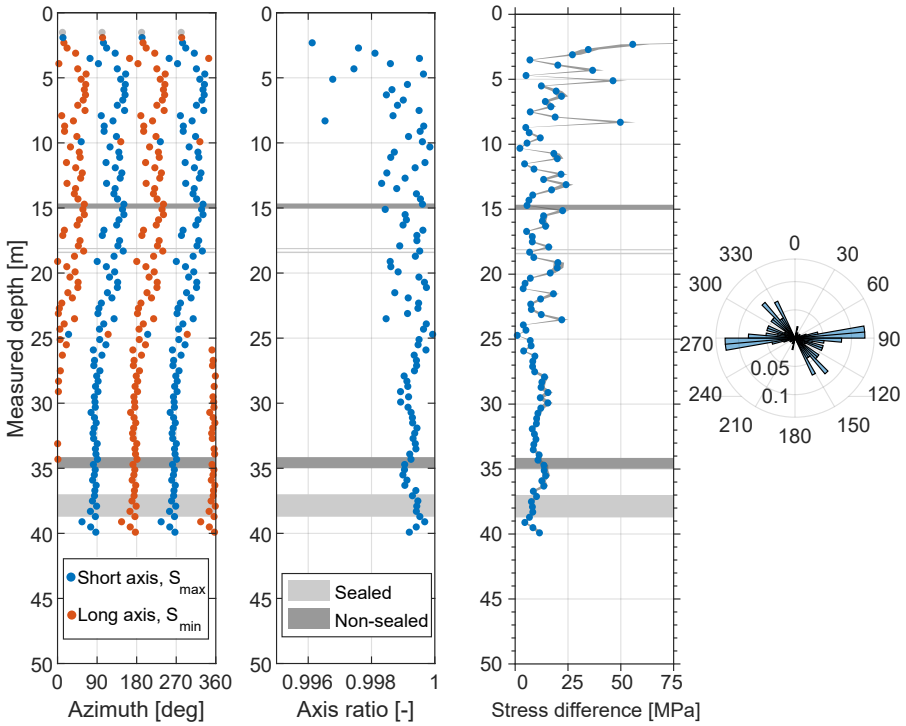

Figure A.7: Ellipticity analysis of SB 2.2 (Data set from 24.02.2019). The rose plots display the short axes of the fitted ellipse. Data points within the casing are colored transparent with grey.

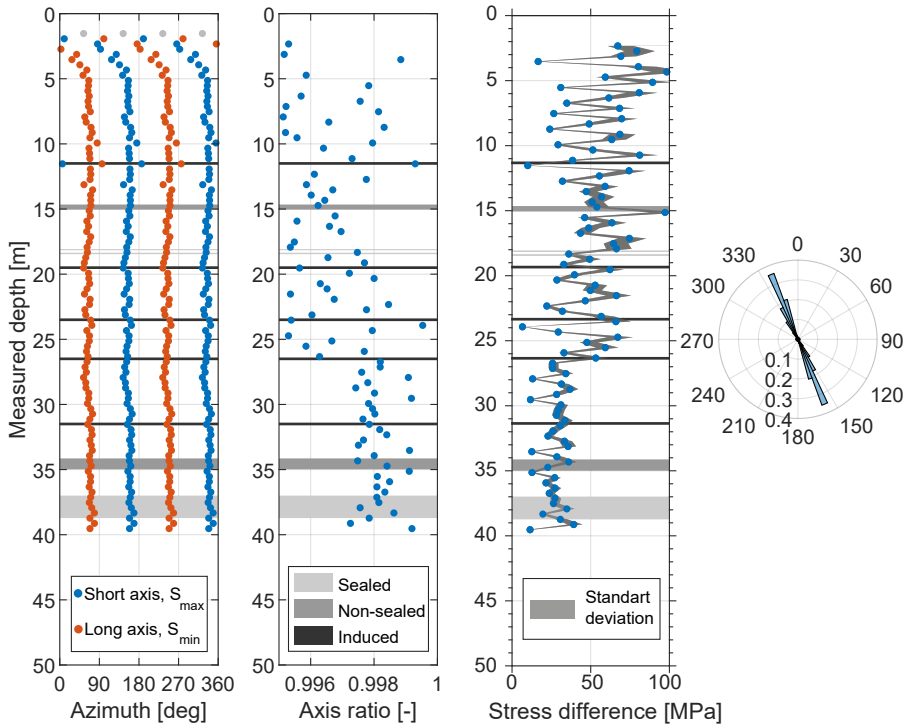

Figure A.8: Ellipticity analysis of SB 2.2 (Data set from 18.04.2019). The rose plots display the short axes of the fitted ellipse. Data points within the casing are colored transparent with grey.

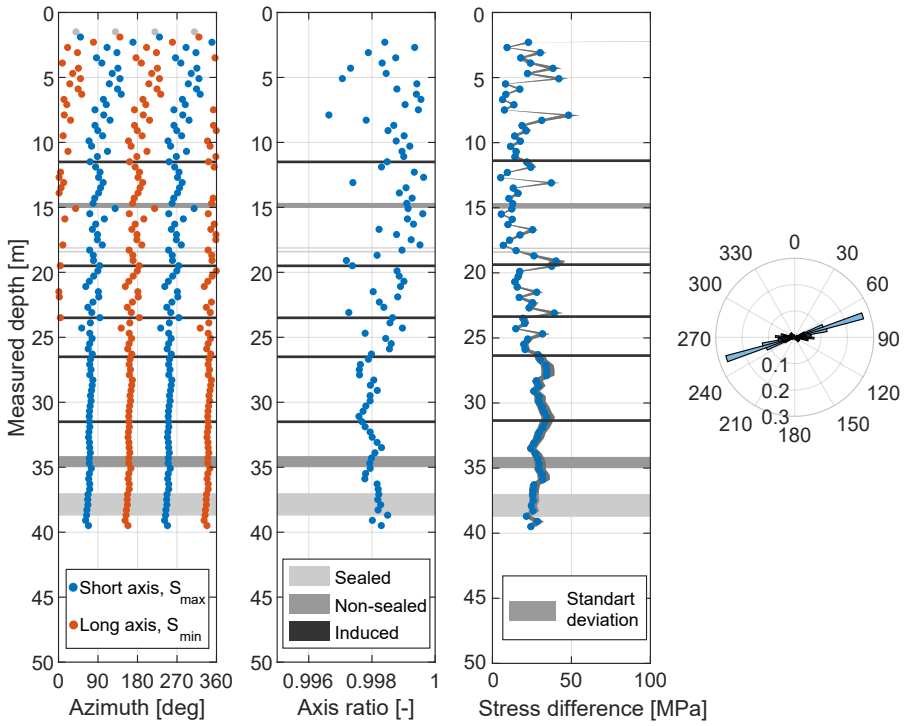

Figure A.9: Ellipticity analysis of SB 2.2 (Data set from 21.04.2019). The rose plots display the short axes of the fitted ellipse. Data points within the casing are colored transparent with grey.

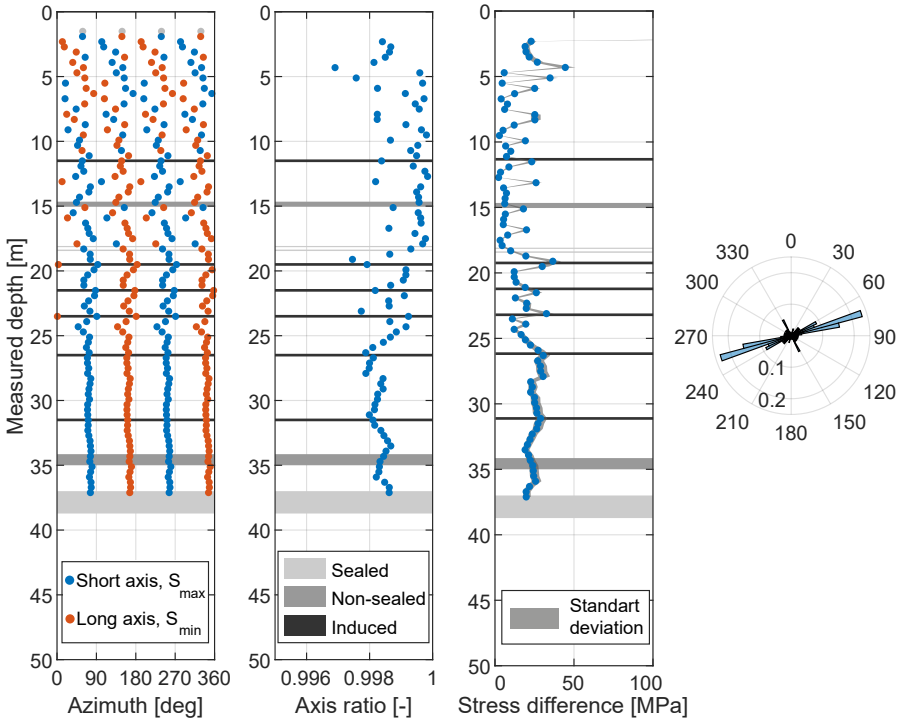

Figure A.10: Ellipticity analysis of SB 2.2 (Data set from 15.07.2019). The rose plots display the short axes of the fitted ellipse. Data points within the casing are colored transparent with grey.

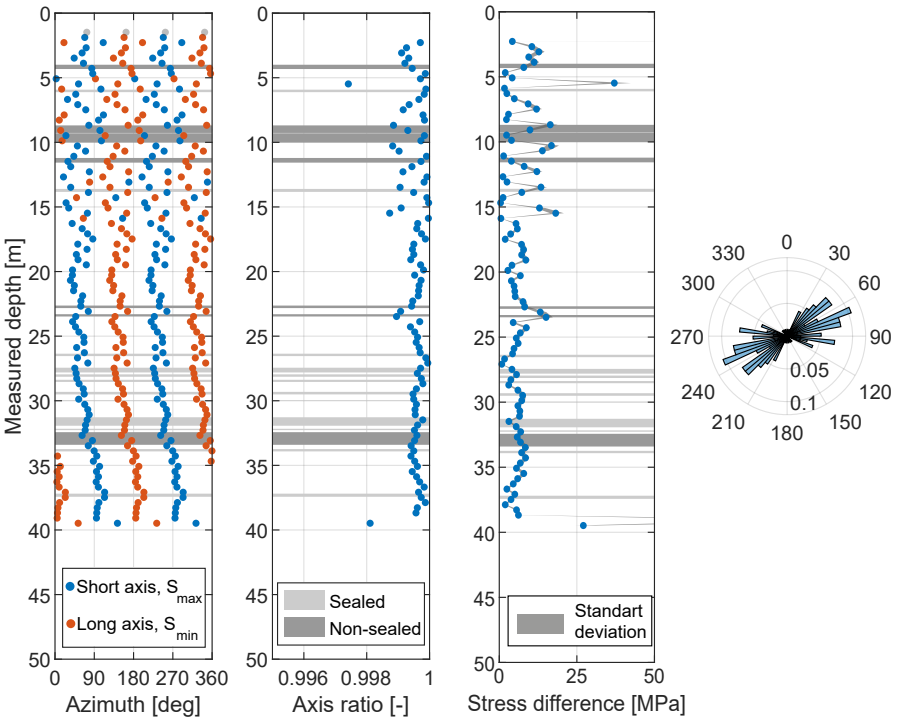

Figure A.11: Ellipticity analysis of SB 2.3 (Data set from 08.03.2019). The rose plots display the short axes of the fitted ellipse. Data points within the casing are colored transparent with grey.

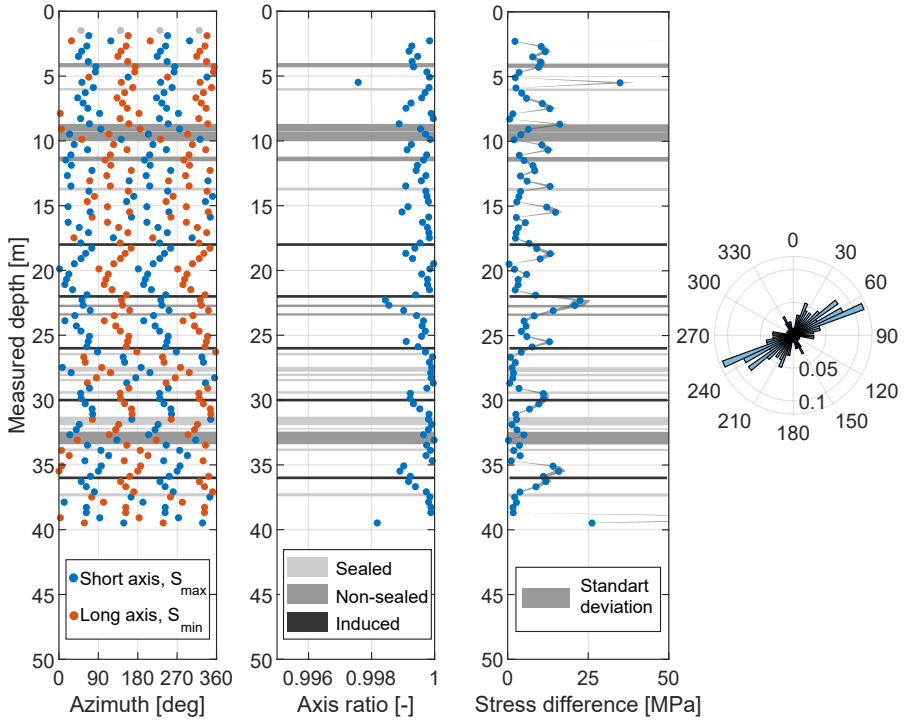

Figure A.12: Ellipticity analysis of SB 2.3 (Data set from 15.07.2019). The rose plots display the short axes of the fitted ellipse. Data points within the casing are colored transparent with grey.

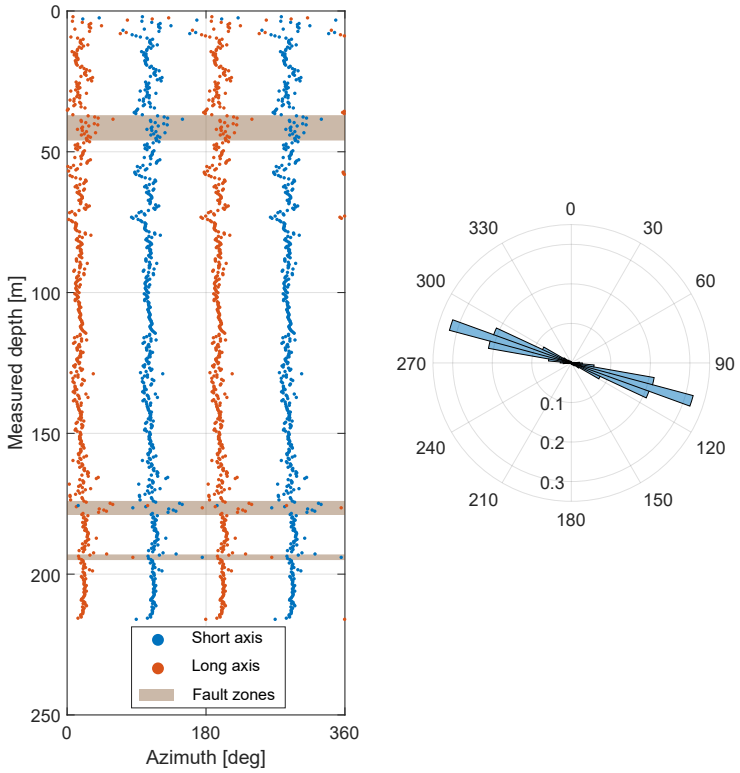

Figure A.13: Ellipticity analysis based on the Amplitude of BFE_A_05. The rose plots display the short axes of the fitted ellipse. Data points within the casing are colored transparent with grey.

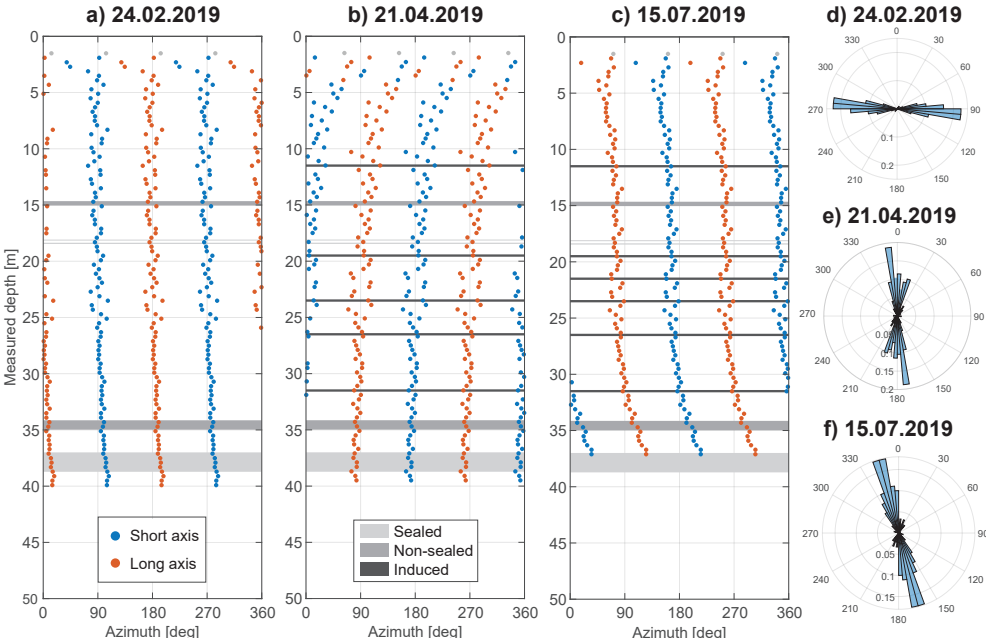

Figure A.14: Ellipticity analysis based on the Amplitude of SB 2.2. The rose plots display the short axes of the fitted ellipse. Figure **a)** and **d)** shows the orientation of the fitted ellipse axes before the Mini-frac tests. While **b)** and **e)** show the data in between the two Mini-frac experiments, when five from six intervals were fractured. **c)** and **f)**) displays the fitted ellipse axes after the Mini-frac tests. Data points within the casing are colored transparent with grey.

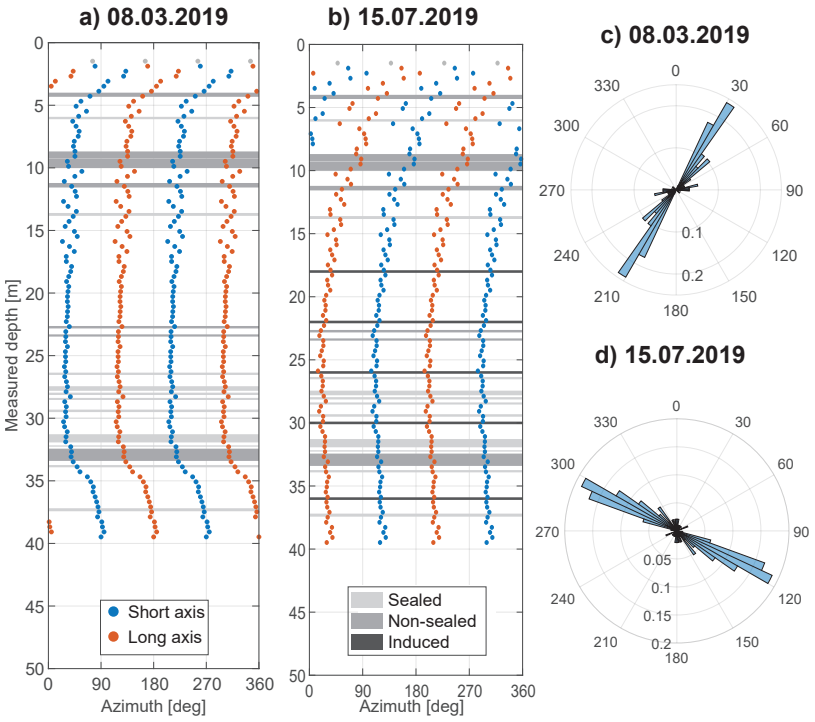

Figure A.15: Ellipticity analysis based on the Amplitude of SB 2.3. The rose plots display the short axes of the fitted ellipse. Whilst **a)** and **c)** shows the orientation of the fitted ellipse axes before the Mini-Frac tests logged by the ATV run at 08.03.2019, **b)** and **d)** show the orientation of the fitted ellipse axes after the Mini-Frac tests from the ATV logging of 15.07.2019. Data points within the casing are colored transparent with grey.

Appendix B

Digital appendix

Further data and figures from the Mini-frac tests and the ATV date are accessible on the following link: https://polybox.ethz.ch/index.php/s/4FXtGStfji2S1E4

1 Mini-frac tests

Figures of the injection protocols in boreholes SB 2.2 and SB 2.3.

2 Borehole logs

PDF and WellCAD files of the ATV data in boreholes SB 2.2 SB 2.3 and BFE_A_05.

Appendix C

Declaration of Originality

Eidgenössische Technische Hochschule Zürich
Swiss Federal Institute of Technology Zurich

Declaration of originality

The signed declaration of originality is a component of every semester paper, Bachelor's thesis, Master's thesis and any other degree paper undertaken during the course of studies, including the respective electronic versions.

Lecturers may also require a declaration of originality for other written papers compiled for their courses.

I hereby confirm that I am the sole author of the written work here enclosed and that I have compiled it in my own words. Parts excepted are corrections of form and content by the supervisor.

Title of work (in block letters):

In situ stress profiling along Bedretto boreholes via integrated geomechanical approaches

Authored by (in block letters):
For papers written by groups the names of all authors are required.

Name(s):	**First name(s):**
Stadler	Deborah

With my signature I confirm that

- I have committed none of the forms of plagiarism described in the 'Citation etiquette' information sheet.
- I have documented all methods, data and processes truthfully.
- I have not manipulated any data.
- I have mentioned all persons who were significant facilitators of the work.

I am aware that the work may be screened electronically for plagiarism.

Place, date	**Signature(s)**
Zurich, 30.11.2022	

For papers written by groups the names of all authors are required. Their signatures collectively guarantee the entire content of the written paper.